HHS Public Access

Author manuscript

Cell Rep. Author manuscript; available in PMC 2021 July 26.

Published in final edited form as:

Cell Rep. 2021 June 29; 35(13): 109293. doi:10.1016/j.celrep.2021.109293.

Breast tumor stiffness instructs bone metastasis via maintenance of mechanical conditioning

Adam W. Watson[1,7], **Adam D. Grant**[1], **Sara S. Parker**[2], **Samantha Hill**[1,2], **Michael B. Whalen**[2], **Jayati Chakrabarti**[1,2], **Michael W. Harman**[3], **Mackenzie R. Roman**[1], **Brittany L. Forte**[1], **Cody C. Gowan**[2], **Raúl Castro-Portuguez**[1], **Lindsey K. Stolze**[2], **Christian Franck**[4], **Darren A. Cusanovich**[2], **Yana Zavros**[1,2], **Megha Padi**[1,5,6], **Casey E. Romanoski**[1,2,8,*], **Ghassan Mouneimne**[1,2,8,9,*]

[1]University of Arizona Cancer Center, Tucson, AZ 85724, USA

[2]Department of Cellular and Molecular Medicine, University of Arizona, Tucson, AZ 85724, USA

[3]School of Engineering, Brown University, Providence, RI 02912, USA

[4]Department of Mechanical Engineering, University of Wisconsin-Madison, Madison, WI 53706, USA

[5]Department of Molecular and Cellular Biology, University of Arizona, Tucson, AZ 85721, USA

[6]Bioinformatics Shared Resource, University of Arizona Cancer Center, Tucson, AZ 85724, USA

[7]MeCo Diagnostics, Tucson, AZ 85718, USA

[8]Senior author

[9]Lead contact

SUMMARY

While the immediate and transitory response of breast cancer cells to pathological stiffness in their native microenvironment has been well explored, it remains unclear how stiffness-induced

*Correspondence: cromanoski@arizona.edu (C.E.R.), gmouneimne@arizona.edu (G.M.).

AUTHOR CONTRIBUTIONS

A.W.W. and G.M. designed the study and wrote the manuscript, with input from all of the authors. A.W.W., M.W.H., S.S.P., M.R.R., B.L.F., C.C.G., R.C.-P., S.H., M.B.W., J.C., and Y.Z. performed and analyzed the cell culture and animal experiments. M.W.H. performed the traction force experiments, while C.F. supervised and contributed intellectually. B.L.F. performed the X-ray analysis. A.W.W. and G.M. conceived of the MeCo scoring metric, and A.D.G., M.P., and G.M. performed the iterative refinement. L.K.S. and C.E.R. performed the RNA-seq and upstream regulator analyses. D.A.C. performed the ATAC-seq analysis. A.D.G. and G.M. performed the analysis of the patient datasets. C.E.R. and G.M. supervised the overall study.

SUPPLEMENTAL INFORMATION

Supplemental information can be found online at https://doi.org/10.1016/j.celrep.2021.109293.

DECLARATION OF INTERESTS

A.W.W. and G.M. have equity in MeCo Diagnostics LLC, which is commercializing the MeCo score under license from the Arizona Board of Regents. G.M. has disclosed an outside interest in MeCo Diagnostics LLC to the University of Arizona. Conflicts of interest resulting from this are being managed by the University of Arizona in accordance with its policies. All of the other authors declare no competing interests.

INCLUSION AND DIVERSITY

One or more of the authors of this paper self-identifies as an underrepresented ethnic minority in science. One or more of the authors of this paper self-identifies as a member of the LGBTQ+ community.

phenotypes are maintained over time after cancer cell dissemination *in vivo*. Here, we show that fibrotic-like matrix stiffness promotes distinct metastatic phenotypes in cancer cells, which are preserved after transition to softer microenvironments, such as bone marrow. Using differential gene expression analysis of stiffness-responsive breast cancer cells, we establish a multigenic score of mechanical conditioning (MeCo) and find that it is associated with bone metastasis in patients with breast cancer. The maintenance of mechanical conditioning is regulated by RUNX2, an osteogenic transcription factor, established driver of bone metastasis, and mitotic bookmarker that preserves chromatin accessibility at target gene loci. Using genetic and functional approaches, we demonstrate that mechanical conditioning maintenance can be simulated, repressed, or extended, with corresponding changes in bone metastatic potential.

Graphical Abstract

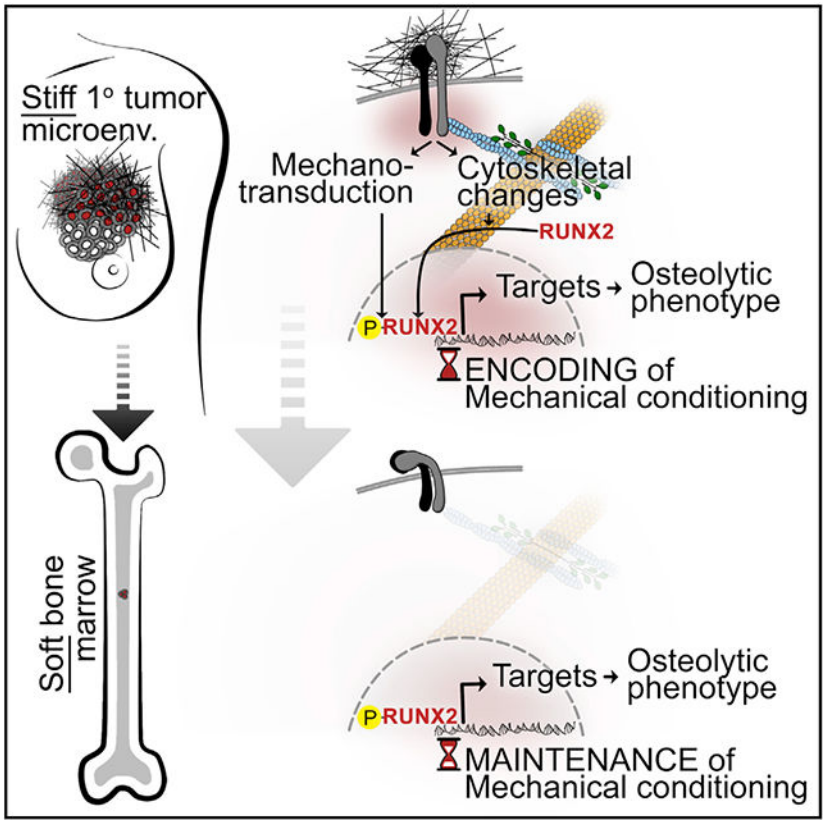

In brief

Watson et al. demonstrate that mechanical conditioning by stiff microenvironments in breast tumors is maintained in cancer cells after dissemination to softer microenvironments, including bone marrow. They show that mechanical conditioning promotes invasion and osteolysis and establish a mechanical conditioning (MeCo) score, associated with bone metastasis in patients.

INTRODUCTION

Tumor stiffening is a ubiquitous feature of breast cancer progression, which produces a varied mechanical landscape ranging from normal elasticity to fibrotic-like tissue stiffness (Plodinec et al., 2012). When cells engage a stiff matrix through focal adhesions, the physical resistance triggers mechanotransduction, defined as a rapid conversion of mechanical stimuli into biochemical signals. Mechanotransduction promotes the first steps of metastasis by increasing cytoskeletal dynamics, cell migration, and invasion *in situ* (Huang et al., 2004). However, the mechanical stimuli that instruct cell behavior in the primary tumor are not persistent throughout the metastatic cascade. This is particularly relevant when metastatic colonization occurs in soft microenvironments such as perisinusoidal bone marrow (BM) (Chen et al., 2020), which constitutes the initial site of tumor outgrowth in breast cancer bone metastasis. Therefore, we sought to determine the extent to which cancer cells maintain their mechanically induced behavior after transition to different mechanical microenvironments.

In this study, we found that cell behaviors associated with invasive and osteolytic activities are induced by stiff matrices and are maintained after cancer cells transition to a soft microenvironment. We found that maintenance of mechanical conditioning is associated with chromatin changes that are only gradually lost upon the removal of mechanical stimulation. We leveraged the well-described osteogenic bookmarking transcription factor (TF) Runt-related transcription factor 2 (RUNX2) as a tool to help delineate some of the dynamic changes in chromatin accessibility that are a function of mechanical conditioning maintenance. Importantly, guided by differential gene expression analysis of stiffness-responsive cells, we generated a molecular signature for assessing mechanical conditioning-associated bone metastases in patients. In concert with previous studies detailing the influence of biochemical properties of the primary tumor stroma on distinct metastatic phenotypes, our findings detailing the influence of mechanical properties support a generalized model of cancer progression in which the integrated properties of the primary tumor microenvironment influence the behavior of cancer cells at the metastatic site.

RESULTS

We screened a panel of breast cancer cell lines and patient-derived xenograft (PDX) primary cells for mechanoresponse to different mechanical microenvironments using stiffness-tuned, collagen-coated hydrogels (Figures 1A and 1B). We used two stiffnesses in these experiments: 8.0 kPa, denoted as Stiff (St), which falls within the relevant range for stiff breast tumors (Plodinec et al., 2012), and 0.5 kPa, denoted as Soft (So), which represents the elasticity of soft tissue (Plodinec et al., 2012). We assessed the mechanoresponse to these two stiffnesses by examining two parameters: (1) mechanosensing, using differential spreading as a readout (Puleo et al., 2019); and (2) mechanotransduction-induced transcription, using expression levels of connective tissue growth factor (CTGF), which is the transcriptional target of the well-established mechanosensitive TF Yes-associated protein (YAP) (Nagelkerke et al., 2015). While all of the cells tested showed elevated mechanoresponse on stiff hydrogels compared to soft, SUM159 cells showed the greatest combined response (Figure 1B). To interrogate mechanical conditioning maintenance, we

developed a multifunctional analysis workflow consisting of an initial phase of mechanical preconditioning, followed by a mechanical conditioning challenge (or control) phase, and then by various functional assays (Figure 1A). We examined the actin cytoskeleton and protrusion dynamics in three experimental groups: stiff-preconditioned control cells (St7/St1), which are cultured on stiff hydrogels for 7 days in phase 1 (St7) and then transferred to new stiff hydrogels for 1 day in phase 2 (St1); soft-preconditioned control cells (So7/So1); and soft-challenged cells (St7/So1), which are stiff-preconditioned cells challenged with 1 day on soft hydrogels before analysis. St7/St1 cells exhibited increased membrane dynamics compared to So7/So1 cells, which maintained reduced dynamics throughout imaging on glass (Figure 1C). Intriguingly, soft-challenged St7/So1 cells fully retained their increased dynamics and behaved similarly to St7/St1 cells (Figures 1C, 1D, S1A, and S1B; Video S1). This was recapitulated in the traction-induced displacement signatures obtained via multidimensional traction force microscopy; however, while the magnitude of traction-induced cell displacements was similar among the St7/St1 and St7/So1 cells (Figures 1E, S1C, and S1D), the polarization of contractility, or average spatial arrangement of tractions, was slightly diminished in both St7/So1 and So7/So1 cells (Figures 1F and S1E). In parallel, we examined the structure of the actin cytoskeleton *in situ* in cells on soft and stiff gels (Figures 1G and S1H). Using the ratio of cortical actin intensity over the intensity of the actin in the rest of the cells (non-cortical), we observed that cells cultured on soft gels exhibit an increase in cortical actin bundles, as compared to stiff. Remarkably, after transitioning to cultures on glass for 1 day (equivalent to the imaging conditions of the experiments described above), the mechanically conditioned cells retained their phenotypic differences. These experiments suggest that mechanical conditioning imparts stable changes in the actin cytoskeleton associated with higher traction and protrusion dynamics.

We examined the associated changes with respect to invasion using a live-cell imaging-based assay, which allowed us to track single-cell migration and translocation of the collective invasion front in 3D. St7/So1 cells exhibited similar invasive activity to St7/St1 cells, as quantified by the number of invading cells (Figures 1I, 1J, and S1F–S1I). Interestingly, although soft-preconditioned (So7/So1) cells invaded less, the translocation of their invasion front was not diminished, compared to the other groups, suggesting that mechanical conditioning maintenance particularly sustained single-cell dissemination (Figure 1K; Video S2). Notably, the behavior associated with mechanical conditioning of the cells was assessed after a period of time that exceeded the average population doubling time (Figure S4D), suggesting that the majority of the cells have undergone at least one cell division at the time of the assay; the changes acquired by mechanical conditioning may persist through cell division and are inherited in daughter cells. These results show that mechanical conditioning maintenance involves perpetuating cell migration phenotypes associated with stiffness-induced invasion.

Furthermore, we investigated the potential relationship between mechanical conditioning and breast cancer outcome in patients. To create an unbiased molecular signature associated with mechanical conditioning, we performed RNA sequencing (RNA-seq) gene expression analysis in SUM159 cells conditioned on soft and stiff matrices for 14 days. Differential expression analysis revealed that 930 genes were upregulated and 1,795 were downregulated by >2-fold on stiff gels at a 5% false discovery rate (FDR) (Figure 2A).

Next, we used these gene sets to generate the mechanical conditioning (MeCo) score. The transcripts used to calculate this score were defined by our RNA-seq analysis, and each patient's MeCo score was calculated using primary tumor expression data; specifically, MeCo scores were calculated by taking the average expression of *in vitro*-upregulated genes (defined by SUM159 differential expression analysis) and subtracting the average expression of *in vitro*-downregulated genes for the expression profile of each primary tumor (key resources table). Furthermore, to mitigate any complicating influence from proliferation (Figure S2D), we excluded transcripts that are known to be strongly associated with proliferation (Selfors et al., 2017) (key resources table). Using the METABRIC 2019 cohort, we found that high MeCo scores are strongly associated with poor overall survival, suggesting that primary tumor stiffness is associated with poor prognosis in general (Figure 2C; hazard ratio [HR] = 2.2, $p < 0.0001$). Furthermore, examination of MeCo scores in the PAM50 tumor subtypes showed that aggressive subtypes, such as basal, human epidermal growth factor receptor 2 (HER2), and luminal B, have strikingly higher average MeCo scores compared to the less aggressive luminal A and normal-like subtypes (Figure S2F); this is consistent with a contrasting expression pattern of PAM50 genes between soft- and stiff-preconditioned cells (Figure S2G). These observations are also consistent with our data showing that stiffness preconditioning enhances invasion.

Interestingly, transcripts upregulated by stiffness preconditioning were enriched for involvement in skeletal ontologies (using Metascape; Tripathi et al., 2015) (Figures 2B andS2A), as well as several skeletal pathologies (using Enrichr; Kuleshov et al., 2016) (Figures S2B and S2C). This led us to prioritize bone metastasis as a stiffness-induced consequence of metastasis-competent cancer cells.

To test for a clinical association between mechanical conditioning and bone metastasis, we used a combined cohort of 560 patients for whom metastasis status/site were recorded. High MeCo scores were strongly associated with lower bone metastasis-free survival (BMFS), compared to low MeCo scores (Figure 2D; HR = 1.6; $p < 0.0001$; Figure S2E). Furthermore, among the 185 patients in the combined cohort who developed bone metastasis, the median time to bone metastasis (TTBM) was 19 months for those with high MeCo scores, compared to 35 months for those with low MeCo scores (Figure 2E). To identify the genes that contribute to the association between MeCo score and bone metastasis independently of subtype and patient cohort, we used linear regression to correct for subtype-specific effects and differences in platform and subtype composition between studies in the combined cohort of 560 patients, used as a training dataset (Figures S2H–S2J), and we found the subset of MeCo genes ($MeCo^{refined}$) that were consistently up- or downregulated between bone-metastatic and non-metastatic primary tumors (Figure S2K; key resources table). As expected, the $MeCo^{refined}$ score was significantly better at assessing BMFS and TTBM than matched gene sets randomly chosen from up- and downregulated genes between bone-metastatic and non-metastatic primary tumors (Figures 2F, 2G, S2L, and S2M). Next, we validated the $MeCo^{refined}$ score in two independent datasets (validation datasets), NKI (HR = 2.1, $p < 0.009$) and METABRIC 2019 (HR = 2.2, $p < 0.0001$) (Figures 2H–2K), showing that a high $MeCo^{refined}$ score is associated with poor bone metastatic outcomes. With respect to different subtypes, although the HRs were significant using $MeCo^{refined}$ score in all of the subtypes in the training dataset (Figures S2N and S2O), they were only significant in the

luminal A and B subtypes in the METABRIC dataset; these results are very intriguing since the luminal breast cancer subtypes have been associated with higher rates of bone metastasis (Metzger-Filho et al., 2013). The data were not significant in the NKI dataset, in part due to the very small number of patients in each group after grouping by subtype (data not shown). In addition, the association of $MeCo^{refined}$ score with brain and lung metastases was not as significant as bone metastasis in the training or validation datasets. These analyses reveal how mechanical conditioning is associated with bone metastasis at the genome-wide level.

To determine whether fibrotic-like stiffness promotes bone metastasis *in vivo*, we injected NOD-*scid IL2rγ*^{null} mice with soft-, stiff- or plastic-preconditioned SUM159 cells in the left cardiac ventricle and tracked bone changes with X-ray imaging. Progressive osteolysis was evident in both the stiff- and plastic-preconditioned groups compared to the soft-preconditioned group (Figures 2L, 2M, and S3A). To test the osteolytic capacity of soft-preconditioned cells and to simultaneously determine whether their colonization deficit was extravasation dependent, we performed intrafemoral injection of St7/So1 or So7/So1 cells to bypass systemic circulation. Soft-challenged St7/So1 cells grew faster *in situ* than So7/So1, and their growth led to reduced cortical bone volume (Figures S3B–S3G). These data support that mechanical conditioning maintenance promotes osteolytic disease *in vivo*.

The reproducible relationship between high MeCo scores and poor bone metastatic outcomes motivated our inquiry into potential TFs that coordinate the transcriptional response to stiffness and could underlie mechanisms of mechanical conditioning. Genes regulated by stiffness in our RNA-seq analysis were filtered using two annotation tools: (1) the Ingenuity Pathway Analysis Upstream Regulator routine that used curated relationships between expression changes and regulators, and (2) vcharacterization in the Human Cancer Metastasis Database (Zheng et al., 2018). This approach prioritized 5 TF candidates: HMGB1, GATA4, RUNX2, CEBPA, and CEBPB (Figure 3A). Next, we used the assay for transposase-accessible chromatin (ATAC-seq) (Buenrostro et al., 2013) to examine the chromatin accessibility landscape during and after transition of SUM159 cells from stiff to soft matrices over a 7-day time course (Figure S4A). We found that the similarity in chromatin accessibility across samples was largely related to the amount of time cells spent on soft matrix after transition from stiff (Figures 3B, S4B, and S4C). We focused on two sets of loci whose accessibility changed upon transition to soft substrate: a “delayed-closing” set, and a “quick-closing” set. The delayed-closing sites are those with no significant decrease in accessibility by day 2 on soft matrix, but with significantly less accessibility by day 5 (defined using a likelihood ratio test framework; see Method details). In contrast, quick-closing sites were those with a significant loss of accessibility after only 12 h in the soft environment. This time frame is shorter than the mean population doubling, mitigating effects of proliferation (Figure S4D). We identified 7,277 delayed-closing genomic regions, which we reasoned should be enriched for regulatory sites responsible for relatively longer-lived expression changes than the quick-closing set. Using genomic region-based pathway enrichment analysis (McLean et al., 2010), we found that genes near these sites are implicated in “abnormal bone remodeling” ($q = 0.015$), among other pathways (key resources table). Motif enrichment analysis of the sequences at these loci revealed that the RUNX consensus binding motif is enriched in delayed-closing ($p = 1e–33$), but not quick-closing sites (Figure 3C); importantly, RUNX binding motifs were also significantly

enriched in sites that maintained their accessibility throughout our time course after transitioning to a soft environment (p = 1e–1,458) (key resources table). In contrast, the consensus binding motif of another bone metastasis regulator, BACH (Liang et al., 2012), is enriched in the quick-closing but not the delayed-closing sites. Together with previous work showing that RUNX2 is an osteogenic TF with genomic bookmarking properties that are associated with bone metastasis (Pratap et al., 2006; Young et al., 2007; Kadauke and Blobel, 2013), these analyses of transcriptomic and epigenomic profiles prioritized RUNX2 as part of the program that regulated mechanical conditioning and its maintenance.

To directly examine the involvement of RUNX2 in maintaining chromatin accessibility after the loss of mechanical stimulation, we again used ATAC-seq in wild-type and RUNX2 knockdown (KD) SUM159 cells (Figure S4E). On day 7 of acclimation to stiff gels, RUNX2 KD and control cells exhibited accessibility differences in only 910 sites (Figure 3D). After 0.5 days of transitioning to soft hydrogels, more genomic loci closed in the RUNX2 KD cells compared to control (53,030 in small hairpin RUNX2 [shRUNX2]; 37,873 in control) (Figures 3D and S4E), supporting a model whereby RUNX2 maintains accessibility during the transition. Motif analysis of the loci differentially open in control cells relative to shRUNX2 cells identified enrichment of the RUNX family motif at all 3 time points ($p < 1e–23$; Figure 3E), demonstrating that RUNX2 maintains accessibility at these sites, with the majority of differential sites occurring at the St7/So0.5 time point (Figures 3E and S4F). Binding sites for activator protein-1 (AP-1) TFs were also among the most enriched in loci enriched in control conditions compared to RUNX2 KD (Figure 3E). AP-1 has been shown previously to function as a collaborative TF in other cell types such as endothelial cells and macrophages (Heinz et al., 2013; Hogan et al., 2017). Importantly, AP-1 has also been shown to interact with RUNX2 at osteogenic genes (Hess et al., 2001; D'Alonzo et al., 2002), and to play an essential role in osteogenic differentiation (Wagner, 2002; Bozec et al., 2010). These results suggest that in a stiff microenvironment, continuous mechanical stimulation could, at least partially, compensate for a lack of RUNX2 expression. However, when cells transition to a soft microenvironment, RUNX2 plays a role, along with other TFs such as AP-1, to maintain accessibility reminiscent of stiff conditioning. Most strikingly, of the control sites with delayed-closing profiles in this experiment (n = 8,560), 28% shifted to quick-closing kinetics upon RUNX2 KD (i.e., closed within the first 12 h). These data reveal for the first time that a temporal profile of chromatin accessibility can be shifted via KD of a mechanically sensitive TF and point toward a distinctive role for RUNX2 in mechanical conditioning maintenance.

In a panel of cell lines and PDX primary cells, we observed increased RUNX2 in stiff-versus soft-preconditioned cells, in both 2D and 3D culture systems (Figures 4A and 4B). We next measured the expression of known RUNX2 target genes (Inman and Shore, 2003; Little et al., 2012; Li et al., 2015) and found that the osteolytic target genes granulocyte-macrophage colony-stimulating factor (GM-CSF), osteopontin (OPN), integrin β-like 1 (ITGBL1), and interleukin-8 (IL-8) were induced by stiffness in a RUNX2-dependent manner (Figures 4C and 4D). Upon removal from stiffness, RUNX2 target transactivation was only gradually lost, concomitant with a gradual increase in Perilipin1 (PLIN1), an adipogenic biomarker (Figure 4E). However, YAP target expression did not persist in a similar way to RUNX2 targets (Figures 4F and S3F), which was surprising since YAP has been linked to mechanical

memory in epithelial cells (Nasrollahi et al., 2017). However, despite being a well-established transducer of mechanical cues, YAP has no known gene bookmarking function (Kadauke and Blobel, 2013; Moroishi et al., 2015).

Mechanistically, we observed increased extracellular signal-regulated kinase 1/2 (ERK) activation on stiff hydrogels, and we confirmed that the expression of RUNX2 targets is down-stream of the stiffness-induced ERK activation of RUNX2; moreover, this was dependent on the activity of the classic mechanotransduction mediators Src and FAK, in addition to the contractile activity of the actomyosin cytoskeleton (Figures 4G–4L). However, inhibition of AKT, another regulator of RUNX2 (Tandon et al., 2014), did not significantly suppress RUNX2 targets at 8 kPa stiffness, although a slight increase in GM-CSF and ITGBL1 expression and a slight decrease in OPN and IL-8 expression in AKT inhibited cells (Figures 4M and 4N).

With respect to localization, RUNX2 was retained in the cytoplasm in both soft-preconditioned cells on glass and soft-cultured cells *in situ*, compared to stiff-preconditioned cells on glass and stiff-cultured cells *in situ* (Figures 5A–5G). This localization pattern was independent of cell spreading, suggesting that it is not due to volume effect (Figures 5H–5K). Importantly, in supraphysiological stiffness-naive HCI-005 PDX primary cells, nuclear RUNX2 was increased on stiff hydrogels compared to soft, demonstrating that this phenotype is not restricted to plastic-tolerant cell lines (Figures 5F and 5G). Lastly, previous studies have demonstrated that RUNX2 is retained in the cytoplasm by stabilized microtubules (Pockwinse et al., 2006); by pharmacologically stabilizing actin or tubulin in stiff-cultured cells or destabilizing the cytoskeleton in soft-cultured cells, we were able to confirm this finding through the expected directional changes in the cytoplasmic retention of RUNX2 (Figures 5L–5O).

We next validated our functional analyses in different breast cancer culture models. In contrast to SUM159 cells, SKBR3 breast cancer cells did not exhibit substantial changes in cytoskeletal dynamics or invasion in response to mechanical conditioning (Figures S5A–S5G). This correlates with their limited tumorigenicity and low metastatic potential *in vivo* (Holliday and Speirs, 2011). We derived a new subline, MS-SKBR3.1 cells, by extended culture in a mechanical sensitization media containing ascorbic acid and phosphate, which are osteogenic factors known to be elevated in breast tumors (Langemann et al., 1989; Bobko et al., 2017). In MS-SKBR3.1 cells, stiffness induced RUNX2 localization to the nucleus, and it triggered mechanical conditioning maintenance that was reflected in cytoskeletal dynamics, RUNX2 target expression, and 3D invasion (Figures S5A–S5J; Videos S4 and S5). These data further illustrate the link between pathological stiffness response, RUNX2 activity, and bone metastatic competency. To further validate the involvement of RUNX2 in mechanical conditioning maintenance, we generated MCF10A-Neu-RUNX2 cells by expressing human RUNX2 in *Neu*-transformed MCF10A cells (Leung and Brugge, 2012), which express low levels of endogenous RUNX2 (Figure S6J). The expression of the osteolytic RUNX2 target genes was induced by exogenous RUNX2 on a stiff substrate and remained significantly elevated after 2 days on soft, compared to 7 days on soft (Figure S5K).

As a bookmarking TF, RUNX2 remains bound to chromatin through mitosis to maintain the cellular phenotype across cell generations (Young et al., 2007). However, without continual activation by matrix stiffness, we reasoned that RUNX2 activity may decrease after multiple cell divisions. Therefore, we hypothesized that mechanical conditioning maintenance may be erased via sufficient proliferation. To test this, we preconditioned cells on stiff hydrogels for 7 days to encode mechanical conditioning, and then we labeled them with CellVue (a membrane dye retention approach to track proliferation) just before switching them to soft hydrogels for 7 days (Figures 6A and S6A). RUNX2 target expression was higher in the low-proliferative St7/So7Cellvue^{HIGH} cells compared to St7/So7Cellvue^{LOW} cells (Figures 6B, S6B, and S6C). In addition, St7/So7Cellvue-HIGH cells retained greater invasive ability than St7/So7Cellvue-LOW cells (Figure 6C–6F; Video S3). To determine whether longer-term "memory" is causally related to reduced proliferation, we pharmacologically reduced cell-cycle progression directly and indirectly. The inhibition of CDK4/6, using palbociclib, extended OPN expression upon removal from stiffness, yet it did not induce expression *de novo* in soft-preconditioned cells that had already lost their conditioning maintenance (Figure 6G). Similar results were obtained when we inhibited DNMT1 using decitabine (Figure 6G), which is also consistent with reports showing that OPN expression is regulated by promoter methylation (Shen et al., 2014). These results suggest that in mechanically sensitive cells, RUNX2 activity is associated with the maintenance of mechanical conditioning, and low-proliferative cells possess more durable mechanical memory.

Next, we investigated the role of RUNX2 in mediating mechanical memory in BM resident cancer cells *in vivo*. Long-term stiff-preconditioned control and RUNX2 KD SUM159 cells expressing GFP were introduced by intraosseous injections; after 1 week, femurs were harvested and cells were flushed out from the BM and sorted by GFP using fluorescence-activated cell sorting (FACS) (Figure 6H). Using ATAC-seq, we examined differential chromatin accessibility and discovered 36,986 significant loci (28,782 with greater accessibility in control; 8,204 with greater accessibility in shRUNX2; Figure 6I), along with enrichment of RUNX and AP-1 motifs in control versus shRUNX2 cells ($p < 1e–91$). Next, we evaluated the differentially accessible sites from this cross-sectional *in vivo* experiment using the patterns of accessibility defined in our earlier *in vitro* longitudinal experiments (e.g., quick versus delayed closing; Figures 3C and S6D). RUNX2 KD cells exhibited a greater proportion of quick-closing signature compared to control cells (Figures 6J and S6D). Notably, RUNX2 target genes contained many reduced accessibility sites (Figures S6E–S6H). These *in vivo* results are consistent with our *in vitro* data and suggest that RUNX2 plays a role in maintaining an epigenome that reflects stiff preconditioning and delayed chromatin remodeling after transition to dissimilar mechanical microenvironments.

To examine the involvement of RUNX2 mechanical induction in osteolytic bone metastasis, we generated RUNX2 functional mutants that are mechanistically linked to the ERK-mediated mechanotransduction pathway. We mutated two crucial ERK phosphorylation sites: RUNX2-S301A-S319A (RUNX2-SA), which is a non-phosphorylatable mutant that is unresponsive to ERK stimulation, and RUNX2-S301E-S319E (RUNX2-SE), which is a phosphomimetic mutant that exhibits high transcriptional activity irrespective of ERK stimulation (Ge et al., 2009). Phosphorylation of these sites by ERK is necessary for previously described chromatin modification by RUNX2 (Li et al., 2017), central to its

known role in transcriptional memory (Zaidi et al., 2010). RUNX2-wild-type (WT) cells had higher RUNX2 target expression on stiff hydrogels compared to soft, indicating that stiffness can activate overexpressed RUNX2-WT; in addition, RUNX2-SE cells on soft hydrogels had partially rescued stiffness-induced target expression, while RUNX2-SA cells on stiff hydrogels had dramatically reduced target expression (Figures 7A and S6I–S6K). These changes in RUNX2 activity were reflected in changes in invasiveness and protrusive activity *in vitro* and in osteolytic bone metastasis after intracardiac injections *in vivo* (Figures 7B–7D, S6L–S6N and S7A–S7E; Video S6). Notably, non-osseous metastases (i.e., lung, liver, and brain) showed dissimilar patterns of disease burden (Figures S7F–S7J). In addition, since RUNX2 targets (particularly OPN) are known to mediate adhesion to bone matrix and to activate osteoclasts (Pratap et al., 2006; Bernards et al., 2008; Feng and Teitelbaum, 2013), we sought to determine how stiffness-activated RUNX2 affected these parameters. Compared to soft-preconditioned, stiff-preconditioned RUNX2-WT cells adhered/spread faster, protruded more on synthetic bone matrix, and induced more paracrine osteoclastogenesis (Figures 7E–7H and S7K–S7O; Video S7). This phenotype was mimicked in soft-preconditioned RUNX2-SE cells and repressed in stiff-preconditioned RUNX2-SA cells, confirming the importance of stiffness-induced phosphorylation in promoting mechanical conditioning maintenance.

DISCUSSION

In our working model, the maintenance of mechanical conditioning is in part mediated by RUNX2, a mechanically sensitive TF (Young et al., 2007; Zaidi et al., 2017). We show that the maintenance of mechanical conditioning involves durable expression of RUNX2 targets that are associated with an osteolytic phenotype after cancer cells transition to softer microenvironments; this diverged from YAP targets, which are downregulated sooner after removal from a stiff matrix. Our results distinguish RUNX2-mediated maintenance of mechanical conditioning from the YAP-mediated mechanical “memory” previously described in cells upon the immediate transition to a softer matrix during cell migration (Nasrollahi et al., 2017).

We demonstrate that RUNX2 is activated by fibrotic-like stiffness, first by nuclear localization following increased cytoskeletal dynamics and then by mechanotransduction via ERK phosphorylation. In addition, we show that the resulting osteolytic phenotype can be mimicked in soft-preconditioned cells with the overexpression of a phosphomimetic RUNX2 mutant or repressed in stiff-preconditioned cells by the overexpression of a non-phosphorylatable RUNX2 mutant. We show that maintenance of this RUNX2-mediated mechanical phenotype corresponds to enhanced invasion, adhesion to synthetic bone matrix, activation of osteoclasts, and promotion of osteolytic bone metastasis. A tangible mechanism by which RUNX2 maintains these mechanically induced traits after transition away from stiff substrates is through its known ability to function as a mitotic bookmarking TF (Young et al., 2007; Zaidi et al., 2017). Mitotic bookmarkers retain their ability to bind key target genes and genomic loci harboring their sequence-specific motifs through mitosis. As such, these TFs provide a beacon for associated chromatin remodelers and assemblage of appropriate transcriptional regulators once mitosis is complete, thereby serving as a mechanism to transmit mechanical memory in the chromatin landscape.

Our data provide insight into the temporal dynamics of mechanical conditioning in breast cancer cells. A similar concept is reported for mesenchymal stem cells, which are able to maintain their mechanically mediated differentiation state after their mechanical microenvironment is altered (Yang et al., 2014; Dingal et al., 2015). However, in contrast to differentiated cells, some cancer cells proliferate rapidly, which contributes to a high susceptibility of losing their phenotypic programs after removal from the encoding microenvironment through proliferative cycles. Apart from phenotypes perpetuated by genetic mutations, maintenance of transcriptional programs by a mechanism such as mechanical conditioning represents an important paradigm for preserving phenotypic programs acquired in the primary tumor. This is particularly relevant in the context of bone metastasis, in which cancer cells may retain their mechanically induced osteolytic capacity during an extended period of slow growth. Thus, breast cancer cells may exploit primary tumor stiffness-induced osteogenic gene bookmarking to direct future bone remodeling upon their exit from dormancy. In some patients, these cells may constitute a subpopulation that has resisted chemotherapy in a soft microenvironment, such as the perisinusoidal BM, which has been shown to promote dormancy (Yeh and Ramaswamy, 2015; Price et al., 2016; Choi and Harley, 2017).

Since bone metastases inflict the greatest morbidity associated with breast cancer and become incurable in a majority of women with advanced disease (Coleman, 2006), it is critical that we strive to predict their genesis. We used an *in vitro* cell system to derive the raw MeCo gene signature, and when applied in an unbiased way to gene expression profiles of primary tumors, we found that high MeCo scores were significantly associated with poor BMFS in clinical datasets. Subsequently, we refined the MeCo score using a training dataset and then validated it in multiple independent datasets. Together with our experimental studies, this clinical analysis provides evidence that the MeCo score is associated with mechanically induced invasive and osteolytic activities, making it a proxy for assessing tumor stiffness response, rather than stiffness itself. This distinction is advantageous, since most invasive breast tumors are stiffer than the surrounding tissue (Evans et al., 2012), yet only a fraction is stiffness responsive and produces osteolytic metastases. Our study furthers our understanding of how mechanical attributes of the primary tumor microenvironment could have prognostic power to identify patients with breast cancer who are at risk of developing bone metastasis, and it supports further development of the MeCo score as a candidate complementary diagnostic to repurpose US Food and Drug Administration (FDA)-approved antifibrotic drugs for bone metastasis prevention.

STAR★METHODS

RESOURCE AVAILABILITY

Lead contact—Correspondence and requests for reagents will be handled by Ghassan Mouneimne (gmouneimne@arizona.edu).

Materials availability—All unique/stable reagents generated in this study are available from the Lead Contact with a completed Material Transfer Agreement.

Data and code availability—The RNA-seq and ATAC-seq data files have been uploaded into the GEO database (GEO: GSE127887).

Tables and uncropped western blots were deposited on Mendeley Data: http://doi.org/10.17632/kvzhkpb8yd.1

EXPERIMENTAL MODEL AND SUBJECT DETAILS

Cell lines—SUM149 and SUM159 cells were cultured in Ham's F12 media (Corning) supplemented with 5% HI-FBS (GIBCO), 5 μg/ml insulin (Roche), 1 μg/ml hydrocortisone (Sigma) and antibiotics (100 units/mL penicillin + 100 μg/ml streptomycin from Life Technologies, Inc.). MDA-MB-231, HEK293T, BT20, T47D, ZR-75–30, MCF7, BT474 and PC3 cells were cultured in DMEM high glucose media (Corning) supplemented with 10% FBS and antibiotics. HCI-005, HCI-011, HCI-003 and were cultured in Mammocult base media (StemCell Technologies, Inc.) supplemented with Mammocult additives. MCF10A cells were cultured in DMEM/F12 media (Corning) with 5% horse serum, 20 ng/ml EGF, 0.5 mg/ml hydrocortisone, 100 ng/ml cholera toxin, 10 μg/ml insulin plus antibiotics. SKBR3 cells were cultured in McCoy's 5A modified media (Corning) supplemented with 10% FBS and antibiotics. MCF10A-Neu cells were a gift from Cheuk Leung (University of Minnesota). MS-SKBR3.1 cells were derived from SKBR3 cells cultured for 6 weeks at 80%–100% confluency in DMEM high glucose media supplemented with 10% FBS, 50 μM ascorbic acid 2-phosphate, and 5 mM disodium glycerol-2-phosphate plus antibiotics (mechanical sensitization media; M.S. media). MS-SKBR3.1 cells were assayed within 2 passages of sensitization. For live-cell imaging experiments, cells were maintained in a climate-controlled chamber (OKO-lab). Cell lines were validated by STR testing (Arizona Cancer Center EMSR core facility) and screened for mycoplasma (Biotool).

Mice—Adult female 6–8 weeks old NOD.Cg-*Prkdc*^{scid} *Il2rg*^{tm1Wjl}/SzJ mice or NOD.Cg-*Prkdc*^{scid}/J (Jax) were randomly allocated into experimental groups. Mice were maintained in pathogen-free conditions and provided with sterilized food and water *ad libitum*. All animal procedures were performed in accordance with the National Research Council's Guide for the Care and Use of Laboratory Animals and were approved by the University of Arizona Institutional Animal Care and Use Committee.

Patient-derived xenografts—Female breast cancer PDX models were established and gifted by Alana Welm (Huntsman Cancer Institute). For propagation of HCI-005, HCI-011 and HCI-003 tumors, 2 mm × 2 mm frozen chunks were implanted subcutaneously in NOD.Cg-*Prkdc*^{scid} *Il2rg*^{tm1Wjl}/SzJ mice and allowed to grow until their diameter exceeded 1.75 cm and necessitated excision, or the animals showed signs of undue pain or distress. *Ex vivo* analysis of PDX cells was done between p4 and p6. To isolate transformed cells, freshly excised tumor chunks were digested with collagenase/hyaluronidase in DMEM (StemCell Technologies, Inc.) for 3 hours at 37°C, using differential adhesion to reduce the proportion of mouse fibroblasts transferred to hydrogels for preconditioning.

METHOD DETAILS

2D hydrogels and 3D conditioning—For mechanical preconditioning, cells were cultured on 2D polyacrylamide, collagen I-conjugated hydrogels, lab-made or purchased (Petrisoft, Matrigen). Soft hydrogels were either 0.5 kPa (Petrisoft) or < 1.0 kPa (lab-made), while stiff hydrogels were either 8.0 kPa (Petrisoft) or lab-made (7.0–8.0 kPa). Prior to making hydrogels, glass coverslips were first pre-treated with a 2% solution of 3-amino-propyltrimethoxy silane (Sigma) in isopropanol, for 10 minutes. After washing, coverslips were treated with 1% Glutaraldehyde for 30 minutes, washed, and dried. To generate the hydrogels, a final ratio of 3/0.055% and 5/0.5% acrylamide/bis-acrylamide were used for < 1.0 kPa and 7–8 kPa hydrogels, respectively. Acrylamide and bis-acrylamide were diluted in 50 mM HEPES (pH 8.5), with 0.1% APS and 0.2% TEMED added to the gel solution. Following polymerization on pre-treated glass coverslips, hydrogels were stored at 4°C in PBS until prepared for matrix coating. For matrix coating, hydrogels were treated with 2 mg/ml Sulfo-SANPAH (Life Technologies) and were placed under long wavelength UV light for 5 minutes. Hydrogels were then washed with PBS and coated with 30 μg/ml rat-tail collagen I (Corning) for 1 hour at 37°C, and then washed with PBS again prior to plating. Cells were fed every 2 days and split/assayed at ~80% confluence. Long-term viability was confirmed with LIVE/DEAD Viability/Cytotoxicity (Thermo Fisher) *in situ* and DAPI exclusion during flow cytometry. For 3D conditioning, cells were grown for 7 days in 1.0 mg/mL rat-tail collagen-I (soft), or 1.0 mg/mL rat-tail collagen-I crosslinked with 0.0175% PEG-di(NHS) (MP Biomedicals) (stiff). Cells were spun down and collected after 20 min incubation in Collagenase type I (0.25%) (StemCell Technologies, Inc.). Hydrogel stiffness was verified by AFM (W.M. Keck Center for Surface and Interface Imaging).

Vectors and virus production—The plasmid pCMV-msRUNX2 (a gift from Gerard Karsenty, Columbia) was used as the source for RUNX2 cDNA, and ERK-target site mutants were made using Quikchange (Agilent): msRUNX2-S301A-S319A (RUNX2-SA) which is unresponsive to ERK stimulation, and msRUNX2-S301E-S319E (RUNX2-SE) which exhibits high basal transcriptional activity in the absence of ERK stimulation (Ge et al., 2009). RUNX2-WT, RUNX2-SA and RUNX2-SE were then subcloned into lentiviral transfer plasmid pCIG3 (Addgene #78264, a gift from Felicia Goodrum, which was first modified to express a puromycin resistance gene in place of GFP). These mutants were used for *in vitro* and *in vivo* analyses (Figures S6 and S7; note that mouse RUNX2 isoforms run slower by SDS-PAGE than endogenous human RUNX2, and mouse RUNX2-SA runs faster than mouse RUNX2-WT and mouse RUNX2-SE). To assay human RUNX2 isoform overexpression we subcloned human RUNX2-I (MRIPV isoform, GeneCopoeia #EX-I2457-Lv105) into pCIB (Addgene #119863), and the human-equivalent ERK-target sites were made using Quikchange and subcloning: wild-type pCIB-hsRUNX2, pCIB-hsRUNX2-S280A-S298A (RUNX2-SA) and hsRUNX2-S280E-S298E (RUNX2-SE) which were used for additional *in vitro* validations (Figures S9B and S9C; note that human RUNX2-SA does not run faster by SDS-PAGE than human RUNX2-WT or human RUNX2-SE, as is observed with mouse isoforms, yet the effects on target gene expression is consistent for both species). For live-cell actin dynamics, we used pLenti Lifeact-iRFP670-BlastR (Addgene #84385). For constitutive activation of MAPK pathway, we used pBabe-Puro-MEK-DD (a gift from William Hahn, Addgene #15268). shRNA for RUNX2 were purchased from

Dharmacon: shRUNX2#01 V2LHS_15065 (TCTGGAAGGAGACCGGTCT); shRUNX2#02 V2LHS_223856 (TACAAATAAATGGACAGTG). For virus production, HEK293T cells were transfected at 60% confluence using Fugene HD (Promega) in OptiMEM (Corning) with transfer plasmid and second-generation lentiviral packaging system (psPAX2 and pMD2.G, Addgene #12260 and #12259, gifts from Didier Trono) or pCL-Ampho (Novus) for lentiviral or retroviral production, respectively. Virus was collected 48–72 hours post-transfection, clarified by 0.45 μm filters. Recipient cells were infected at 50% confluence with virus at a 1:1 dilution with culturing media and polybrene (10 μg/mL). Puromycin selection was started 48 hours post-infection.

Cytoskeletal dynamics—After mechanical preconditioning, SUM159, SKBR3 and MS-SKBR3.1 cells expressing iRFP-LifeAct were trypsizined from their hydrogels and plated onto No. 1.5 glass MatTek dishes which had been pre-treated overnight with DMEM + 10% FBS, and then incubated for 10 hours to ensure maximal spreading before analysis (verified by size equilibrium). Cytoskeletal dynamics score was obtained by automatic tracing of iRFP signal and averaging single-cell displacement over three sequential 1 hour intervals. Imaging was acquired with a 20X Plan Apo 0.75 N objective (Nikon) and an ORCA-Flash 4.0 V2 cMOS camera (Hamamatsu).

Multidimensional traction force—Cells were mechanically preconditioned as indicated, and then plated onto 1.7 kPa or 8.5 kPa bead-embedded collagen I-coated hydrogels (30 μg/ml), prepared as detailed above. Imaging commenced 4 hours after plating onto bead-embedded hydrogels that were either 1.7 kPa or 8.5 kPa. Fluorescent microsphere beads (0.5 μm; Life Technologies) were dispersed throughout the hydrogels and excited with a red HeNe diode (561 nm) laser. PKH67-stained cells were visualized with an Argon (488 nm) laser. Three-dimensional image stacks were acquired using a Nikon A-1 confocal system mounted on a Ti-Eclipse inverted optical microscope controlled by NIS-Elements Nikon Software. A Plan Fluor 40X air 0.6 N objective (Nikon) mounted on a piezo objective positioner was used, which allowed imaging speeds of 30 frames per second using a resonant scanner. Confocal image stacks of 512 × 512 × 128 voxels (108 × 108 × 38 μm^3) were recorded every 30 min with a z-step of 0.30 μm. Cell-induced full-field displacements were measured as previously described (Toyjanova et al., 2014) using the FIDVC algorithm (Bar-Kochba et al., 2015).

3D organotypic invasion assay—The invasion assays were modified from Padilla-Rodriguez et al. (2018). Briefly, for SUM159 experiments, 75,000 preconditioned single cells were suspended in a dome of 15 μL Matrigel (Corning), spotted onto silanized 8-well coverslip chamber slides (LabTek), incubated for 30 min, and then embedded in 1 mg/mL neutralized rat tail collagen-I (Fisher) crosslinked with 0.0125% PEG-di(NHS) (MP Biomedicals) (see Figure 1A). Imaging was performed in a 16 hours period, starting 18 hours after embedding. For SKBR3 and MS-SKBR3.1 experiments 180,000 cells were suspended and embedded as above, and then imaging was performed immediately for 24 hours. Invaded cells which divided during the imaging periods were counted as one cell in order to mitigate any differences in proliferation among experimental groups. Invasion front translocation was calculated by tracking the midpoint of the cluster of cells at the

Matrigel:collagen interface which align perpendicular to the direction of movement using DIC cell tracking in Elements software (Nikon). Imaging was acquired with a 20X Plan Apo 0.75 N objective (Nikon) and an ORCA-Flash 4.0 V2 cMOS camera (Hamamatsu).

RNA-seq library preparation, sequencing, and normalization—SUM159 cells were cultured for 2 weeks on collagen I-conjugated hydrogels that reflect native human breast tumor stiffness corresponding to regions of high cellularity/low matrix deposition (0.5 kPa; Petrisoft, Matrigen), versus low cellularity/high matrix deposition (8.0 kPa; Petrisoft, Matrigen) (Plodinec et al., 2012). Cells were fed every 2 days and were split or analyzed when 80% confluent. 3 biological replicates of each stiffness were processed for RNA extraction using Isolate II RNA kit (Bioline), and 1μg from each sample was used for polyA selection with [Oligo d(T) Magnetic Beads, New England BioLabs #S1419S]. mRNA was converted into sequencing libraries as previously detailed (Hogan et al., 2017). In brief, RNAs were fragmented and ligated to barcoded adapters (Bioo Scientific, NEXTflex DNA Barcodes). Quantitative RT-PCR was used to determine the optimal number of cycles to amplify each library as to achieve sufficient DNA quantity while maintaining the diversity of the library (10–20 cycles). Libraries were then amplified, and fragments with insert sizes between 225 and 375 bp were isolated by gel purification, pooled at equimolar concentrations, and submitted for massively parallel high-throughput sequencing (single end, 50 base pairs) on a Hi-Seq4000 (Illumina) at the University of Chicago's Genomics Core using manufacturer protocols.

RNA-seq differential expression, pathway enrichment, and upstream regulator analyses—De-multiplexed fastq files were mapped to the human transcriptome (hg38) in STAR (Dobin et al., 2013) using default settings and organized into tag directories using makeTagDirectory in the HOMER (Heinz et al., 2010) software suite. The number of mapped, uniquely aligned reads suggested good coverage of the transcriptome and diversity in the sample set. Hierarchical clustering recapitulated that samples clustered by group membership, as expected, confirming that differences in transcriptomes were driven by cellular matrix environments.

Differential gene expression was calculated in DESeq (Anders and Huber, 2010) using a 5% False Discovery Rate (FDR) as defining the differential gene set. Pathway enrichment analysis was performed in Metascape (Tripathi et al., 2015) using additional 4-fold cutoffs to define up- and downregulated genes between soft and stiff samples. Upstream Regulatory analysis was performed on differentially expressed genes using a more inclusive 2-fold cutoff with Ingenuity Pathway Analysis (IPA) software (QIAGEN), which returns a list of genes having enriched curated connections to the input gene set as a method to predict upstream regulators. Candidate regulators were restricted to genes having receptor or transcription factor function because these provide a straightforward mechanism for how the mechanical stiffness signal may become integrated in cells to cause differential gene expression. Candidate upstream regulators with prediction $p < 0.05$ were exported and intersected with the gene set annotated as "Metastasis Associated Genes" from the Human Cancer Metastasis Database (Zheng et al., 2018). From this list of intersecting genes, we then manually searched the literature for those with gene bookmarking function or

"transcriptional memory" association. We do not exclude the possibility that we may have missed some epigenetic memory-associated genes that are not well curated. For gene ontologies associated with the stiffness-induced gene set, we also used Enrichr (Kuleshov et al., 2016), through query of the Human Phenotype Ontology (Köhler et al., 2014) and MGI Mammalian Phenotype (Blake et al., 2009) libraries.

Mechanical conditioning (MeCo) scoring and patient data analysis—The initial gene set for MeCo scoring was derived from RNA-seq differential expression between SUM159 cells grown on stiff versus soft hydrogels for 2 weeks. Genes that had $P_{adj} < 0.05$ and $|\log_2 FC| > 1$ were considered differentially expressed (FC = fold change). After removing genes associated with proliferation (Selfors et al., 2017), there were a total of 3,822 remaining differentially expressed genes. Out of these genes, 1,143 had a positive $\log_2 FC$ while 2,679 had a negative $\log_2 FC$. Genes with a positive $\log_2 FC$ were considered to be associated with stiffness, while genes with a negative $\log_2 FC$ were associated with softness.

We queried three microarray studies from the Gene Expression Omnibus (GEO) to test the clinical association between mechanical conditioning and bone metastasis: GSE2034, GSE2603, GSE12276. Studies GSE2034 and GSE2603 were sequenced using the Affymetrix Human Genome U133A array, and study GSE12276 was sequenced using the Affymetrix Human Genome U133 Plus 2.0 array. The normalized expression matrix was downloaded from GEO using the R GEOquery package and all values were $\log_2$ transformed. In addition, breast tumor samples that underwent sequencing in multiple GEO studies were treated as a single sample (Bos et al., 2009). After merging the studies GSE2034, GSE2603, GSE12276 together, there were 12,403 overlapping genes. Out of these 12,403 genes, 2,210 genes were in common with the 3,822 RNA-seq differentially expressed genes. 711 out of the 2,210 genes were associated with stiffness and 1,409 out of the 2,210 were associated with softness (Figure S3A). In conjunction, we used the METABRIC 2019 (molecular dataset) in our analysis to act as an independent study. There were 2,949 genes that overlapped with the RNA-seq gene signature and the METABRIC dataset (942 stiff-associated and 2,007 soft-associated) (Figure S3B).

MeCo score calculation for each patient was performed by taking the average gene expression differences between stiff- and soft-associated genes: [mean expression (stiff genes) – mean expression (soft genes)]. Unlike gene signatures normally used to define cancer subtypes, the MeCo score is patient-specific, so the expression profiles of other samples within the same study do not affect the MeCo score. Moreover, because the MeCo signature subtracts normalized contributions from two sets of genes, any chip- or batch-specific effect that is gene-independent will automatically cancel, making it more robust and transferable across studies (Altenbuchinger et al., 2017). Thus, we combined MeCo scores from the GSE2034, GSE2603, GSE12276 studies and were able to increase the power of our analysis. Notably, we are assuming that the Affymetrix Human Genome U133A array and the Affymetrix Human Genome U133 Plus 2.0 array share similar probe affinities for genes that are in common between arrays.

To optimize the utility of the MeCo score, we refined the RNA-seq gene signature by identifying the overlapping genes that are associated with stiffness or softness, and that are positively and negatively associated with bone metastasis in the three GEO studies described above. The R package *limma* was used to calculate $\log_2$FC between patients who are bone metastasis positive and patients who are bone metastasis negative, while controlling for study and subtype in a linear regression framework. Tumor subtypes were identified using the PAM50 signature from the R package *genefu*. This analysis produced 1,051 genes upregulated with bone metastases and 1,069 genes downregulated with bone metastases. Of the 1,051 upregulated genes, 323 were associated with stiffness. Of the 1,069 downregulated genes, 681 were associated with softness. In total, there are 1,004 genes in the refined MeCo score. Furthermore, 919 genes from this refined MeCo score overlapped with the genes represented in the METABRIC expression study and were used to reassess overall survival in that cohort.

The genes used for MeCo score calculations are listed in the key resources table. For proliferation scoring, we used the normalized, average gene expression of the proliferation-associated genes (Selfors et al., 2017) listed in the key resources table.

Two independent datasets were used to validate the $\text{MeCo}^{\text{refined}}$ score: the NKI dataset from van de Vijver et al. (2002) and the METABRIC 2019 (Rueda et al., 2019). Note that for the bone metastasis-free survival (BMFS) analysis using the METABRIC 2019, out of the patient subset with gene expression data (METABRIC molecular dataset), we selected all patients with complete recurrence history (Complete.Rec.History = YES). In this analysis, patients with no bone metastasis were censored using their TDR data, which is time until last follow-up or distant relapse; patients with no distant relapse (DR = 0) were assumed to not having bone metastasis. Time-to-bone-metastasis (TTBM) analysis was performed using all patients with bone metastasis.

Furthermore, we wanted to test whether mechanical conditioning contributes significantly to the power of the $\text{MeCo}^{\text{refined}}$ score, or whether our results are simply driven by the gene expression patterns observed in bone metastasis positive and negative tumors. Motivated by the methodology in Venet et al. (2011), we generated 1,000 matched random gene sets and compared their performance against $\text{MeCo}^{\text{refined}}$. Each gene set initially consisted of 2,120 randomly selected genes to mimic the original MeCo gene set. To simulate the calculation of the $\text{MeCo}^{\text{refined}}$ score for each of the 1,000 random gene sets, we used the same linear regression analysis between bone metastasis positive and bone metastasis negative samples as before. For each gene set, the top 1,004 genes were ranked and separated based on positive $\log_2$FC and negative $\log_2$FC from the regression analysis. Positive genes were considered to be associated with stiffness and negative genes were associated with softness. The randomized versions of the refined MeCo scores were calculated by taking the difference between the mean gene expression of stiff genes and the mean gene expression of soft genes. Distributions of the log rank statistic of BMFS and TTBM for the randomized gene sets were created using the combined cohort of 560 patients. The log rank statistics for both BMFS and time-to-BM computed from the true $\text{MeCo}^{\text{refined}}$ gene signature were significantly higher than expected from matched random gene sets ($p < 0.05$ and $p < 0.001$).

Assay for transposase accessible chromatin (ATAC-seq)—We collected chromatin accessibility data genome-wide across a 7-day time course of transitioning cells from stiff to soft substrates using the assay for transposase accessible chromatin ('ATAC-seq'). ATAC-seq was performed on 50,000 SUM159 cells using the previously described protocol (Corces et al., 2017). Libraries were run on a 10% TBE gel and DNA from 175–225 bp was extracted for sequencing. For each time point, triplicate experiments were conducted to allow for quantitative comparisons of accessibility across the time course. After generating libraries, samples were equimolar pooled and sequenced on an Illumina NextSeq High output run (single-end 75bp). After filtering out poor samples based on basic quality control, we retained triplicates for 12 hours after transition (St7/So0.5), 1 day (St7/So1), 2 days (St7/So2), and 5 days (St7/So5), and 2 replicates for the 7-day time point (St7/So7); the third replicate from this time point was excluded because of low sequencing depth (< 300,000 unique, autosomal mapped reads versus > 6,000,000 for all other samples) and low fraction of reads in peaks called on the sample (0.24 versus 0.39–0.63 for all others). In addition, we retained triplicates for two sets of control samples that were maintained on stiff substrate for 1 day and 7 days after the initial 7-day preconditioning on stiff substrate (St7/St1 and St7/St7, respectively). We then identified peaks of accessibility (also called "hypersensitive sites") on each sample to generate a genome-wide map of accessible regulatory elements using MACS2 (Zhang et al., 2008). To compare the similarity of peaks identified in each time point, we used BEDTools (Quinlan and Hall, 2010) to calculate all pairwise Jaccard indices and generated a heatmap with the 'heatmap.2′ function in the 'gplots' package in R. To allow for quantitative comparisons in accessibility between time points we generated a master list of peaks, taking the union of all peaks identified in each of the time points and then counted how many reads mapped to each peak for each sample. These values were normalized for read depth by dividing by how many million reads were contained in the union peak set for each sample. Finally, the read depth-normalized values were $\log_{10}$-transformed (after adding a small constant) and median normalized. Principal component analysis of this matrix confirmed that time was a major predictor of quantitative differences in accessibility for sites common to all samples. A likelihood-ratio test framework was used to identify sites that were differentially accessible in one of the soft matrix time points relative to all of the stiff matrix controls:

$$Y_{ij} = \mu_i + \beta_i X_j + \varepsilon_{ij}$$

Y_{ij} represents the accessibility of site i for sample j, μ_I is the mean accessibility for site i, X_j is the status of sample j ("soft" versus "control"), β_i is the effect of time spent on soft substrate on accessibility of site i, and ε_{ij} is an error term. For each site, we compared a model with a "soft vs control" term to a nested model with just an intercept using a likelihood-ratio test. P values were adjusted for multiple comparisons using the q-value calculation in the 'qvalues' package in R (Storey and Tibshirani, 2003). For this analysis we focused particularly on quick changing versus delayed changing sites. Sites that we characterized as 'quick' are those that exhibited differential accessibility at 12 hours after transitioning to soft substrate; we identified 7,607 sites that became more accessible and 2,430 sites that became less accessible at 12 hours (at a false discovery rate or 'FDR' of 1%). Sites that we characterized as 'delayed' are those that did not change for the first 2

days but then changed accessibility by days 5 and 7. To determine the delayed sites, we first identified sites that were significantly differentially accessible by day 5 and 7 (at an FDR of 1%) and then excluded any sites that were also identified at any of the earlier time points (at a relaxed FDR of 10%); this analysis yielded 9,816 sites that became more accessible and 7,277 sites that became less accessible. Importantly, the delayed sites would include regulatory elements for genes exhibiting transcriptional memory.

ATAC-seq of RUNX2-knockdown breast cancer cells *in vitro* and *in vivo*— SUM159 cells were infected with either GIPZ (non-targeting control) or shRUNX2#02 expressing lentivirus (n = 3 independent virus preparations each) and selected for 1 week with puromycin. 40,000 cells were plated on soft of stiff hydrogels (22 mm × 22 mm) with media changes every other day, and passaged at 80% confluency. Cells were switched to new hydrogels and then lysed according to the mechanical conditioning schedule detailed in each figure. For *in vivo* experiments, cells were mechanically conditioned for 7 days on stiff hydrogels prior to 1×10^5 cells (in 10 μL PBS) being injected into the intramedullary space of the right distal femur of each *Prkdc*^{scid} mouse (n = 3 mice per group). After cells were conditioned *in vivo* for 7 days, mice were sacrificed and PBS was used to flush bone marrow from the femurs as previously described (Ray et al., 2015). GFP$^+$ SUM159 cells were sorted on a BD FACSAria III using FACSDiva software and processed for ATAC-SEQ as detailed above. Raw sequence reads were trimmed for sequencing adapters, mapped to the hg38 genome using Bowtie2, duplicate reads were removed using HOMER's tags per basepair (tbp) option, and mitochondrial genome reads were removed. Resulting analysis were performed using HOMER's subroutines as follows. ATAC-seq peaks were identified using 'findPeak's using default parameters with the following exceptions: -style histone, 75 bp seed peak size, 75bp minimum distance between peaks, and at least 8-fold enrichment over local background tags. Peaks across all replicates and conditions were merged using 'mergePeaks' and the master peak set was annotated using 'annotatePeaks.pl' to count logged-mean normalized (to 10^6 reads per experiment) values across all conditions. Differential peaks were identified using getDifferentialPeaks between pairwise conditions, requiring at least a 1.7-fold change in normalized counts and 10^{-6} p value (poisson distribution) for differential accessibility. Motif analysis of differential peaks were performed using 'findMotifsGenome.pl' in the sequence set of 100 base pairs flanking peak centers with random genomic sequences of the same size and average GC content used for null expectations. Principal Component (PC) Analysis was performed on the output of 'annotatePeaks.pl' in R using prcomp().

Pathway enrichment analysis of ATAC-seq data—In order to ascertain whether differentially accessible sites for each of the dynamic patterns (quick and delayed closing) were enriched near genes in specific pathways we used the Genomic Regions Enrichment of Annotations Tool ('GREAT'; McLean et al., 2010). For both the quick closing and delayed closing sites (defined above), we uploaded a bed file of all sites passing the respective thresholds to http://great.stanford.edupublic/html and used the whole genome as the background to look for ontology enrichments using the default settings.

Motif enrichment analysis—*De novo* motif analysis of ATAC-seq-defined regions was performed using the HOMER software suite (Heinz et al., 2010), for subsets of open chromatin regions. Regions unchanged after transitioning to a soft matrix after seven days were open chromatin regions that were not in the ‘quick’ or ‘delayed’ closing set. Specifically, enrichments were determined using the findMotifsGenome.pl command with region sizes of 100 basepairs (bp). For quick and delayed changed sites, unchanged sites were used as the background. For unchanged sites, GC-matched 100-bp random genome sequences were used as background.

Immunofluorescence—For RUNX2 localization, cells were preconditioned for 7 days on soft or stiff hydrogels, passaged at ~80% confluence, with media changes every other day. Where drug treatments are indicated, cells were treated with either 1 μg/mL lysophosphatidic acid (LPA; indirect Rho kinase activator; Sigma), 10 ug/mL Rho Activator II (Cytoskeleton Inc.), 20 μM Y27632 (ROCK inhibitor; Sigma), 50 nM jasplakinolide (actin filament stabilizer; Sigma), 1 μM taxol (microtubule stabilizer; Sigma), 30 μM blebbistatin (Myosin II inhibitor; Sigma), 10 μM nocodazole (microtubule destabilizer; Sigma), or 0.1% DMSO for 3 hours in fresh growth media, and then fixed in 4% paraformaldehyde for 20 min at 37°C. Cells were permeabilized in 0.5% TX-100 for 20 min, and blocked for 1H at RT in 5% goat serum + 0.5% BSA in PBS with DAPI (Sigma) and 2% phalloidin-647 (Invitrogen). Cells were then incubated with primary antibodies for 2 hours at RT, and secondary antibodies for 1 hour at RT. The antibodies used were RUNX2 (Sigma Prestige HPA022040 1:250), Tubulin (Sigma T9026 1:250), Human Cytokeratin (Dako clones AE1/AE3 1:250), Paxillin (BD 612405 1:200), phosphoFAK (Thermo 44–625G 1:200), Alexa Fluor goat anti-rabbit 568 1:250 (Invitrogen) and Alexa Fluor goat anti-mouse 488 1:250 (Invitrogen). Samples were mounted in ProLong Diamond Antifade (Thermo-Fisher) and allowed to cure for at least 24 hours before imaging. Image segmentation was performed on the nuclear (DAPI-stained) image for each field. The cytosolic region was defined as a 2.2 μm wide annulus surrounding the nuclear region using Elements software (Nikon).

Immunoblotting—For mechanotransduction experiments, 250,000 cells were plate on 8.5 cm circular hydrogels, media changed every other day, and passaged at ~80% confluence. Protein lysates were resolved with SDS-PAGE and transferred to nitrocellulose. For ERK immunoblots, the following drugs were added along with fresh media 1 hour before lysis: 20 μM PD98059 (MEK inhibitor; Tocris), 30 μM blebbistatin (Myosin II inhibitor; Sigma), 100 nM dasatinib (Src inhibitor; Tocris) and 1 μM Faki14 (Fak inhibitor; Tocris) or 0.1% DMSO. For mechanical memory extension, cells were preconditioned as above with the following drugs: 2 μM palbociclib (CDK4/6 inhibitor; Sigma), 7 μM decitabine (DNMT inhibitor; Sigma), or 0.1% DMSO. Cells were lysed 36 hours after the last media change in RIPA buffer (1% NP-40, 150 mM NaCl, 0.1% SDS, 50 mM Tris-HCl pH 7.4, 0.5% sodium deoxycholate) supplemented with Halt protease inhibitor cocktail (Pierce) and Halt phosphatase inhibitor cocktail (Pierce). For AKT inhibition cells were conditioned on stiff hydrogels for 7 days with drug changes every other day (1 μM MK-2206; Cayman Chemical). Membranes were blocked in 100% Odyssey Blocking Buffer PBS (LI-COR), incubated with primary antibodies overnight at 4°C in 50% blocking buffer + 50% PBST, and secondary antibodies for 1 hour at RT in 50% blocking buffer + 50% PBST. The

antibodies used were RUNX2 (Sigma Prestige HPA022040 1:1000 and Cell Signaling Technology 8486S 1:1000), OPN (Abcam ab8448 1:1000 and Abcam ab91655 1:1000), ERK (Santa Cruz sc-93-G 1:1000), phospho-ERK (Cell Signaling Technology 4377S 1:1000), AKT (Cell Signaling Technology 2920S 1:1000), phosphor-AKT (Cell Signaling Technology 4058S 1:1000), Actin (ProteinTech Group 66009–1 1:5,000), Alexa Fluor goat anti-rabbit 680 1:10,000 (Invitrogen) and Alexa Fluor goat anti-mouse 790 1:10,000 (Invitrogen).

Flow cytometry and sorting—Cells were preconditioned on stiff hydrogels for 7 days to encode mechanical memory, and then labeled with CellVue Claret far-red membrane label (Sigma), using 4 μL label in 200 μL Dil C per 1.0×10^6 cells, before transfer to soft hydrogel conditioning for another 7 days. Cells were fed every 2 days and were split/analyzed when ~80% confluent. Cell sorting was performed on a BD FACSAria III using FACSDiva software. The sequential gating strategy is outlined in Figure S7A. Compensation was done for each experiment using unstained cells and cells stained with individual fluorophores. After sorting, 100,000 cells from $CellVue^{HIGH}$ or $CellVue^{LOW}$ gates were returned to 22 mm × 22 mm soft hydrogels in order to generate conditioned media for 24 hours, before assaying OPN and GM-CSF protein expression, or 3D invasion. Flow cytometry was performed on a BD FACSCanto II. To quantify OPN expression, 1 hour room temperature incubation with OPN-PE (Abcam ab210835, 1:2500) or IgG control (Abcam ab72465, 1:2500) was used following −20°C 90% methanol fixation/permeabilization and blocking in 10% goat serum for 30 min at RT. Flow cytometry data were analyzed using FlowJo using unstained samples to set gates.

Quantitative real-time PCR—For RUNX2 knockdown experiments, cells were infected with either GIPZ (non-targeting control), shRUNX2#01 or shRUNX2#02 expressing lentivirus (n = 3 independent virus preparations each) and selected for 1 week with puromycin. 40,000 cells were plated on soft of stiff hydrogels (22 mm × 22 mm) with media changes every other day, and passaged at 80% confluency. For mechanical memory experiments, cells were plated/passaged as above, and cells were lysed 36 hours after last media change. For mechanotransduction drug treatments, cells were treated with either 30 μM blebbistatin (Sigma), 100 nM dasatinib (Tocris), 1 μM Faki14 (Tocris) on collagen I-coated (or 0.1% DMSO on poly-D lysine-coated) hydrogels for 7 days with media/drug change every other day, including the day before analysis. Total RNA was isolated using Isolate II RNA kit (Bioline) and cDNA was then synthesized from 1μg of RNA using XLA script cDNA kit (Quanta BioSciences). Sybr green PCR mix (Bioline) was used for RT-qPCR on the ABI Fast 7500 system Samples were run in triplicates in each experiment and relative mRNA levels were normalized to housekeeping gene EEF1A. Melt curve analysis was performed to verify that each SYBR reaction produced a single PCR product. All SYBR assays were performed using the following PCR cycling conditions: denaturation at 95°C for 15 min followed by 40 cycles of denaturing at 95°C for 10 sec, and annealing at 60°C for 1 min. See STAR methods Key Resources table for a list of all primers used.

Combined mechanoresponse assay—All cell lines and patient-derived xenografts were mechanically-conditioned for 36 hours on 0.5 kPa (Petrisoft) or 8.0 kPa (Petrisoft)

hydrogels before analysis. Cells were imaged *in situ* using a 10X Plan Apo 0.75 N objective (Nikon) and an ORCA-Flash 4.0 V2 cMOS camera (Hamamatsu). Manual tracing was done to quantify cell spreading on each stiffness. After image acquisition, RT-qPCR analysis of CTGF was performed as detailed above.

Enzyme-linked immunosorbent assay (ELISA)—SUM159 cells were preconditioned for 7 days on stiff hydrogels to encode mechanical memory, and then 500,000 cells were transferred to 8.5 cm soft hydrogels. Media was changed the next day, and then 24 hours after that conditioned media (CM) was collected (2-day-soft CM), spun down to remove cells/debris and snap frozen. Cells were counted and then 500,000 cells were re-plated. This cycle was repeated to generate 4-, 6-, and 8-day soft CM. A GM-CSF Human SimpleStep ELISA kit was used per manufacturer's instructions (Abcam). The colorimetric signal was normalized to total protein lysates from 25% of the cells on the hydrogels after each 2-day conditioning cycle (Coomassie Plus; Pierce). For mechanical memory selection, 100,000 $CellVue^{HIGH}$ or $CellVue^{LOW}$ cells were returned to 22 mm × 22 mm soft hydrogels for 24 hours in order to generate conditioned media (see Flow Cytometry and Sorting), and GM-CSF levels were interpolated from a standard curve per manufacturer's instructions.

Quantification of human cancer cells in mouse tissues—Fresh brain, liver, and lung tissue was snap frozen and stored at −20°C. Whole organs were pulverized after liquid nitrogen treatment, and 20 mg from each was processed for gDNA using GeneJet genomic DNA purification kit (Thermo).The following previously validated primers were purchased from IDT: Human Alu, Fw: YB8-ALU-S68 5′-GTCAGGAGATCGAGACCATCCT-3′, Rev: YB8-ALU-AS244 5′-AGTGGCGCAATCTCGGC-3′, Probe: YB8-ALU-167 5′−6-FAM-AGCTACTCGGGAGGCTGAGGCAGGA-ZEN-IBFQ-3′ (Preston Campbell et al., 2015). Mouse Actb PrimeTime Std (Mm.PT.39a.22214843.g) was used as an endogenous control to normalize each sample. All TaqMan assays were performed using the same PCR cycling conditions as listed above.

Synthetic bone matrix adhesion and spreading—Osteo Assay surface (synthetic bone matrix) 24-well microplates (Corning) were used. For adhesion, 24 hour-old preconditioned media from corresponding experimental groups were collected, and then 200 μL was pre-absorbed to the Osteo plates for 1 hour prior to adding 1.0×10^6 cells in 100 μL fresh media, and incubated for 30 min. Plates were gently tapped to remove loosely bound cells, and the remaining cells were stained with DAPI and enumerated by microscopy with large-stitch imaging using a 10X Plan Apo 0.75 N objective (Nikon) and an ORCA-Flash 4.0 V2 cMOS camera (Hamamatsu). For spreading measurements on synthetic bone matrix, the above protocol was used except imaging commenced immediately upon addition of cells to the plate. Cell area was quantified at 6 min intervals by manual tracing in Elements software (Nikon), using a 20X Plan Apo 0.75 NA objective (Nikon) and a CoolSNAP MYO CCD camera (Photometrics).

Osteoclastogenesis *in vitro*—Osteoclast precursor RAW 264.7 cells were induced for 4 days in 24-well plates with DMEM + 10% FBS + 50 ng/mL RANKL (Sigma) (growth media), and then cultured with 50% cancer cell preconditioned media (CM) + 50% growth

media for another 3 days. CM was collected 24 hours after addition to plates with equal cell counts from each experimental group. Tartrate-resistant acid phosphatase staining was done using the Acid Phosphatase, Leukocyte (TRAP) kit (Sigma) according to manufacturer's instructions. Multinuclear cells that stained positive were enumerated in large-stitched images taken with a 10X Plan Apo 0.75 N objective (Nikon) and a DS-Fi2 color CCD camera (Nikon).

Peripheral blood mononuclear cells (PBMCs) were extracted from the whole blood using Lymphoprep™(STEMCELL Technologies) density gradient medium. Briefly, the blood was diluted 50% v/v in blood wash (1% FCS in DPBS) and added to Lymphoprep™ in a SepMate™ 50-IVD (STEMCELL Technologies) 50mL tubes. The diluted blood was centrifuged at 1200 ×g for 10 mins and the top layer was collected carefully. The leukocyte-enriched supernatant was diluted 50% v/v with blood wash and centrifuged at 300 ×g for 8 mins. The supernatant was discarded, and pellet was resuspended in 10mL Blood wash, followed by a centrifugation at 120 ×g for 10mins in order to separate leukocytes from platelets. The pellet was resuspended in macrophage media (DMEM high glucose 1X, 10% Fetal Calf Serum, 1% P/S) supplemented with 100ng/mL human MCSF (Peprotech, AF-300–25). 50% of the exhausted media was replaced with fresh media on day 3 and supplemented with 100ng/mL human MCSF. On day 6, MCSF was withdrawn from the culture. The differentiated macrophages were treated with DMEM + 10% FBS + 50 ng/mL RANKL (Sigma) (growth media) and then cultured with 50% cancer cell preconditioned media (CM) + 50% growth media for 3 days. Osteoclast clusters were counted in large-stitched images taken with a 10X Plan Apo 0.75 N objective (Nikon) and a DS-Fi2 color CCD camera (Nikon).

Experimental metastasis—In the intracardiac injection model, 2×10^5 SUM159, SUM159-RUNX2-WT, SUM159-RUNX2-SA or SUM159-RUNX2-SE cells (preconditioned for 7 days on soft hydrogels, stiff hydrogels, or TC plastic, as indicated) were injected (resuspended in 100 μL PBS) into the left cardiac ventricle. Upon harvest, non-osseous tissues were flash frozen for subsequent DNA extraction and human *Alu* quantification. In the intraosseous injection model, SUM159 cells were first preconditioned for 7 days on either soft or stiff hydrogels, then re-plated onto new soft hydrogels for 24 hours prior to 5×10^4 cells (in 5 μL PBS) being injected into the intramedullary space of the right distal femur of each animal. All animal studies were approved by the Institutional Animal Care and Use Committee at the University of Arizona.

Bioluminescence *in vivo*—Once a week, mice were injected with 120 mg/kg luciferin and metastatic dissemination was monitored using AMI X (Spectral Instruments). Mice were killed by CO_2 asphyxiation 3–4 weeks after tumor cell injection. Metastatic burden was quantified using AMIView (Spectral Instruments). Exclusion criteria for data analysis were pre-established such that those mice terminated before defined experimental endpoints, for ethical reasons or premature death, were not included in analysis. Investigators were blinded to experimental groups during acquisition of bioluminescence data.

X-ray imaging—Mice were anesthetized with 80 mg/kg ketamine to 12 mg/kg xylazine (in a 10 mL/kg volume) and radiographs were obtained (Faxitron). Data were analyzed with

ImageJ using pixels^2 as the unit of measurement. Investigators were blinded to experimental groups during acquisition and analysis of X-ray data.

Micro-CT imaging—Legs were removed from euthanized mice and fixed in neutral-buffered formalin for 24 hours, then dissected free of tissue and scanned on a Siemens Inveon micro-CT at 80 kV with a 0.5 mm filter, using an effective pixel size of 28 microns. The scanned images were reconstructed with Inveon Research Workplace (Siemens) using the Feldkamp algorithm and Shepp-Logan filter. In the intracardiac injection model, bone parameters were determined in the distal femur, starting 3 mm from the growth plate to the top of the epiphysis. In the intraosseous model, cortical bone thickness, volume, and surface area were determined in a 4 mm length of mid-shaft femur; trabecular bone analysis was excluded in the intraosseous model due to potential destruction caused by the syringe. In order to delineate bone marrow, trabecular bone, and cortical bone, signal threshold intervals were set identically for all specimens. All histomorphometric parameters were based on the report of the American Society for Bone and Mineral Research nomenclature (Parfitt et al., 1987), and analyses were performed as previously described (Sugiyama et al., 2010; He et al., 2017; Eyre et al., 2019). Investigators were blinded to experimental groups during acquisition and analysis of micro-CT data.

QUANTIFICATION AND STATISTICAL ANALYSIS

Sample sizes were determined based on our previous experience with similar experiments (a minimum of 3 to 5 mice for animal studies, or 2 to 4 biological replicates for *in vitro*/*ex vivo* assays). Statistical significance was assessed with GraphPad Prism 8, using the appropriate tests as listed in each figure legend. For analysis patient survival data, we used Kaplan-Meier plots and the Wilcoxon test. Sample sizes and p values are listed in each figure legend.

Supplementary Material

Refer to Web version on PubMed Central for supplementary material.

ACKNOWLEDGMENTS

The authors wish to acknowledge the following: The Experimental Mouse Resource Service, particularly Gillian Paine-Murrieta and Bethany Skovan, for their technical assistance; Brenda Baggett for micro-computed tomography (CT) imaging; John Fitch, Mark Curry, and John Davies for FACS assistance; and Michael Whalen and Lindsey Stolze for data processing. This research was supported by NCI grant R01 CA196885-01 (to G.M.), NHLBI grant R00 HL123485 (to C.E.R.), NIAID grant R01 AI116629-01A1 (to C.F.), the Timothy and Diane Bowden Fellowship (to A.W.W.), NHLBI R01 HL147187 (for C.E.R.), NIH/T32 HL007249-42 and American Heart Association predoctoral fellowship 20PRE35200195 (for L.K.S.), and the NCI University of Arizona Cancer Center Support Grant P30 CA023074.

REFERENCES

Altenbuchinger M, Schwarzfischer P, Rehberg T, Reinders J, Kohler CW, Gronwald W, Richter J, Szczepanowski M, Masqué-Soler N, Klapper W, et al. (2017). Molecular signatures that can be transferred across different omics platforms. Bioinformatics 33, i333–i340. [PubMed: 28881975]

Anders S, and Huber W (2010). Differential expression analysis for sequence count data. Genome Biol. 11, R106. [PubMed: 20979621]

Bar-Kochba E, Toyjanova J, Andrews E, Kim K-S, and Franck C (2015). A Fast Iterative Digital Volume Correlation Algorithm for Large Deformations. Exp. Mech 55, 261–274.

Bernards MT, Qin C, and Jiang S (2008). MC3T3-E1 cell adhesion to hydroxyapatite with adsorbed bone sialoprotein, bone osteopontin, and bovine serum albumin. Colloids Surf. B Biointerfaces 64, 236–247. [PubMed: 18420388]

Blake JA, Bult CJ, Eppig JT, Kadin JA, and Richardson JE; Mouse Genome Database Group (2009). The Mouse Genome Database genotypes:phenotypes. Nucleic Acids Res. 37, D712–D719. [PubMed: 18981050]

Bobko AA, Eubank TD, Driesschaert B, Dhimitruka I, Evans J, Mohammad R, Tchekneva EE, Dikov MM, and Khramtsov VV (2017). Interstitial Inorganic Phosphate as a Tumor Microenvironment Marker for Tumor Progression. Sci. Rep 7, 41233. [PubMed: 28117423]

Bos PD, Zhang XH, Nadal C, Shu W, Gomis RR, Nguyen DX, Minn AJ, van de Vijver MJ, Gerald WL, Foekens JA, and Massagué J (2009). Genes that mediate breast cancer metastasis to the brain. Nature 459, 1005–1009. [PubMed: 19421193]

Bozec A, Bakiri L, Jimenez M, Schinke T, Amling M, and Wagner EF (2010). Fra-2/AP-1 controls bone formation by regulating osteoblast differentiation and collagen production. J. Cell Biol 190, 1093–1106. [PubMed: 20837772]

Buenrostro JD, Giresi PG, Zaba LC, Chang HY, and Greenleaf WJ (2013). Transposition of native chromatin for fast and sensitive epigenomic profiling of open chromatin, DNA-binding proteins and nucleosome position. Nat. Methods 10, 1213–1218. [PubMed: 24097267]

Chen X, Hughes R, Mullin N, Hawkins RJ, Holen I, Brown NJ, and Hobbs JK (2020). Mechanical Heterogeneity in the Bone Microenvironment as Characterized by Atomic Force Microscopy. Biophys. J 119, 502–513. [PubMed: 32668233]

Choi JS, and Harley BAC (2017). Marrow-inspired matrix cues rapidly affect early fate decisions of hematopoietic stem and progenitor cells. Sci. Adv 3, e1600455. [PubMed: 28070554]

Coleman RE (2006). Clinical features of metastatic bone disease and risk of skeletal morbidity. Clin. Cancer Res 12, 6243s–6249s. [PubMed: 17062708]

Corces MR, Trevino AE, Hamilton EG, Greenside PG, Sinnott-Armstrong NA, Vesuna S, Satpathy AT, Rubin AJ, Montine KS, Wu B, et al. (2017). An improved ATAC-seq protocol reduces background and enables interrogation of frozen tissues. Nat. Methods 14, 959–962. [PubMed: 28846090]

D'Alonzo RC, Selvamurugan N, Karsenty G, and Partridge NC (2002). Physical interaction of the activator protein-1 factors c-Fos and c-Jun with Cbfa1 for collagenase-3 promoter activation. J. Biol. Chem 277, 816–822. [PubMed: 11641401]

Dingal PCDP, Bradshaw AM, Cho S, Raab M, Buxboim A, Swift J, and Discher DE (2015). Fractal heterogeneity in minimal matrix models of scars modulates stiff-niche stem-cell responses via nuclear exit of a mechanorepressor. Nat. Mater 14, 951–960. [PubMed: 26168347]

Dobin A, Davis CA, Schlesinger F, Drenkow J, Zaleski C, Jha S, Batut P, Chaisson M, and Gingeras TR (2013). STAR: ultrafast universal RNA-seq aligner. Bioinformatics 29, 15–21. [PubMed: 23104886]

Evans A, Whelehan P, Thomson K, McLean D, Brauer K, Purdie C, Baker L, Jordan L, Rauchhaus P, and Thompson A (2012). Invasive breast cancer: relationship between shear-wave elastographic findings and histologic prognostic factors. Radiology 263, 673–677. [PubMed: 22523322]

Eyre R, Alférez DG, Santiago-Gómez A, Spence K, McConnell JC, Hart C, Simões BM, Lefley D, Tulotta C, Storer J, et al. (2019). Microenvironmental IL1β promotes breast cancer metastatic colonisation in the bone via activation of Wnt signalling. Nat. Commun 10, 5016. [PubMed: 31676788]

Feng X, and Teitelbaum SL (2013). Osteoclasts: New Insights. Bone Res. 1, 11–26. [PubMed: 26273491]

Ge C, Xiao G, Jiang D, Yang Q, Hatch NE, Roca H, and Franceschi RT (2009). Identification and functional characterization of ERK/MAPK phosphorylation sites in the Runx2 transcription factor. J. Biol. Chem 284, 32533–32543. [PubMed: 19801668]

He F, Chiou AE, Loh HC, Lynch M, Seo BR, Song YH, Lee MJ, Hoerth R, Bortel EL, Willie BM, et al. (2017). Multiscale characterization of the mineral phase at skeletal sites of breast cancer metastasis. Proc. Natl. Acad. Sci. USA 114, 10542–10547. [PubMed: 28923958]

Heinz S, Benner C, Spann N, Bertolino E, Lin YC, Laslo P, Cheng JX, Murre C, Singh H, and Glass CK (2010). Simple combinations of lineage-determining transcription factors prime cis-regulatory

elements required for macrophage and B cell identities. Mol. Cell 38, 576–589. [PubMed: 20513432]

Heinz S, Romanoski CE, Benner C, Allison KA, Kaikkonen MU, Orozco LD, and Glass CK (2013). Effect of natural genetic variation on enhancer selection and function. Nature 503, 487–492. [PubMed: 24121437]

Hess J, Porte D, Munz C, and Angel P (2001). AP-1 and Cbfa/runt physically interact and regulate parathyroid hormone-dependent MMP13 expression in osteoblasts through a new osteoblast-specific element 2/AP-1 composite element. J. Biol. Chem 276, 20029–20038. [PubMed: 11274169]

Hogan NT, Whalen MB, Stolze LK, Hadeli NK, Lam MT, Springstead JR, Glass CK, and Romanoski CE (2017). Transcriptional networks specifying homeostatic and inflammatory programs of gene expression in human aortic endothelial cells. eLife 6, e22536. [PubMed: 28585919]

Holliday DL, and Speirs V (2011). Choosing the right cell line for breast cancer research. Breast Cancer Res. 13, 215. [PubMed: 21884641]

Huang C, Jacobson K, and Schaller MD (2004). MAP kinases and cell migration. J. Cell Sci 117, 4619–4628. [PubMed: 15371522]

Inman CK, and Shore P (2003). The osteoblast transcription factor Runx2 is expressed in mammary epithelial cells and mediates *osteopontin* expression. J. Biol. Chem 278, 48684–48689. [PubMed: 14506237]

Kadauke S, and Blobel GA (2013). Mitotic bookmarking by transcription factors. Epigenetics Chromatin 6, 6. [PubMed: 23547918]

Köhler S, Doelken SC, Mungall CJ, Bauer S, Firth HV, Bailleul-Forestier I, Black GC, Brown DL, Brudno M, Campbell J, et al. (2014). The Human Phenotype Ontology project: linking molecular biology and disease through phenotype data. Nucleic Acids Res. 42 (D1), D966–D974. [PubMed: 24217912]

Kuleshov MV, Jones MR, Rouillard AD, Fernandez NF, Duan Q, Wang Z, Koplev S, Jenkins SL, Jagodnik KM, Lachmann A, et al. (2016). Enrichr: a comprehensive gene set enrichment analysis web server 2016 update. Nucleic Acids Res. 44 (W1), W90–W97. [PubMed: 27141961]

Langemann H, Torhorst J, Kabiersch A, Krenger W, and Honegger CG (1989). Quantitative determination of water- and lipid-soluble antioxidants in neoplastic and non-neoplastic human breast tissue. Int. J. Cancer 43, 1169–1173. [PubMed: 2732005]

Leung CT, and Brugge JS (2012). Outgrowth of single oncogene-expressing cells from suppressive epithelial environments. Nature 482, 410–413. [PubMed: 22318515]

Li X-Q, Du X, Li D-M, Kong P-Z, Sun Y, Liu P-F, Wang Q-S, and Feng Y-M (2015). Molecular and Cellular Pathobiology ITGBL1 Is a Runx2 Transcriptional Target and Promotes Breast Cancer Bone Metastasis by Activating the TGFb Signaling Pathway. Cancer Res. 75, 3302–3313. [PubMed: 26060017]

Li Y, Ge C, and Franceschi RT (2017). MAP Kinase-Dependent RUNX2 Phosphorylation Is Necessary for Epigenetic Modification of Chromatin During Osteoblast Differentiation. J. Cell. Physiol 232, 2427–2435. [PubMed: 27514023]

Liang Y, Wu H, Lei R, Chong RA, Wei Y, Lu X, Tagkopoulos I, Kung SY, Yang Q, Hu G, and Kang Y (2012). Transcriptional network analysis identifies BACH1 as a master regulator of breast cancer bone metastasis. J. Biol. Chem 287, 33533–33544. [PubMed: 22875853]

Little GH, Noushmehr H, Baniwal SK, Berman BP, Coetzee GA, and Frenkel B (2012). Genome-wide Runx2 occupancy in prostate cancer cells suggests a role in regulating secretion. Nucleic Acids Res 40, 3538–3547. [PubMed: 22187159]

McLean CY, Bristor D, Hiller M, Clarke SL, Schaar BT, Lowe CB, Wenger AM, and Bejerano G (2010). GREAT improves functional interpretation of cis-regulatory regions. Nat. Biotechnol 28, 495–501. [PubMed: 20436461]

Metzger-Filho O, Sun Z, Viale G, Price KN, Crivellari D, Snyder RD, Gelber RD, Castiglione-Gertsch M, Coates AS, Goldhirsch A, and Cardoso F (2013). Patterns of recurrence and outcome according to breast cancer subtypes in lymph node-negative disease: results from international breast cancer study group trials VIII and IX. J. Clin. Oncol 31, 3083–3090. [PubMed: 23897954]

Moroishi T, Hansen CG, and Guan K-L (2015). The emerging roles of YAP and TAZ in cancer. Nat. Rev. Cancer 15, 73–79. [PubMed: 25592648]

Nagelkerke A, Bussink J, Rowan AE, and Span PN (2015). The mechanical microenvironment in cancer: how physics affects tumours. Semin. Cancer Biol 35, 62–70. [PubMed: 26343578]

Nasrollahi S, Walter C, Loza AJ, Schimizzi GV, Longmore GD, and Pathak A (2017). Past matrix stiffness primes epithelial cells and regulates their future collective migration through a mechanical memory. Biomaterials 146, 146–155. [PubMed: 28918264]

Padilla-Rodriguez M, Parker SS, Adams DG, Westerling T, Puleo JI, Watson AW, Hill SM, Noon M, Gaudin R, Aaron J, et al. (2018). The actin cytoskeletal architecture of estrogen receptor positive breast cancer cells suppresses invasion. Nat. Commun 9, 2980. [PubMed: 30061623]

Parfitt AM, Drezner MK, Glorieux FH, Kanis JA, Malluche H, Meunier PJ, Ott SM, and Recker RR (1987). Bone histomorphometry: standardization of nomenclature, symbols, and units. Report of the ASBMR Histomorphometry Nomenclature Committee. J. Bone Miner. Res 2, 595–610. [PubMed: 3455637]

Plodinec M, Loparic M, Monnier CA, Obermann EC, Zanetti-Dallenbach R, Oertle P, Hyotyla JT, Aebi U, Bentires-Alj M, Lim RY, and Schoenenberger CA (2012). The nanomechanical signature of breast cancer. Nat. Nanotechnol 7, 757–765. [PubMed: 23085644]

Pockwinse SM, Rajgopal A, Young DW, Mujeeb KA, Nickerson J, Javed A, Redick S, Lian JB, van Wijnen AJ, Stein JL, et al. (2006). Microtubule-dependent nuclear-cytoplasmic shuttling of Runx2. J. Cell. Physiol 206, 354–362. [PubMed: 16110492]

Pratap J, Lian JB, Javed A, Barnes GL, van Wijnen AJ, Stein JL, and Stein GS (2006). Regulatory roles of Runx2 in metastatic tumor and cancer cell interactions with bone. Cancer Metastasis Rev. 25, 589–600. [PubMed: 17165130]

Preston Campbell J, Mulcrone P, Masood SK, Karolak M, Merkel A, Hebron K, Zijlstra A, Sterling J, and Elefteriou F (2015). TRIzol and Alu qPCR-based quantification of metastatic seeding within the skeleton. Sci. Rep 5, 12635. [PubMed: 26271202]

Price TT, Burness ML, Sivan A, Warner MJ, Cheng R, Lee CH, Olivere L, Comatas K, Magnani J, Kim Lyerly H, et al. (2016). Dormant breast cancer micrometastases reside in specific bone marrow niches that regulate their transit to and from bone. Sci. Transl. Med 8, 340ra73.

Puleo JI, Parker SS, Roman MR, Watson AW, Eliato KR, Peng L, Saboda K, Roe DJ, Ros R, Gertler FB, and Mouneimne G (2019). Mechanosensing during directed cell migration requires dynamic actin polymerization at focal adhesions. J. Cell Biol 218, 4215–4235. [PubMed: 31594807]

Quinlan AR, and Hall IM (2010). BEDTools: a flexible suite of utilities for comparing genomic features. Bioinformatics 26, 841–842. [PubMed: 20110278]

Ray P, Stacer AC, Fenner J, Cavnar SP, Meguiar K, Brown M, Luker KE, and Luker GD (2015). CXCL12-γ in primary tumors drives breast cancer metastasis. Oncogene 34, 2043–2051. [PubMed: 24909174]

Rueda OM, Sammut SJ, Seoane JA, Chin SF, Caswell-Jin JL, Callari M, Batra R, Pereira B, Bruna A, Ali HR, et al. (2019). Dynamics of breast-cancer relapse reveal late-recurring ER-positive genomic subgroups. Nature 567, 399–404. [PubMed: 30867590]

Selfors LM, Stover DG, Harris IS, Brugge JS, and Coloff JL (2017). Identification of cancer genes that are independent of dominant proliferation and lineage programs. Proc. Natl. Acad. Sci. USA 114, E11276–E11284. [PubMed: 29229826]

Shen C-J, Tsou YA, Chen HL, Huang HJ, Wu SC, Cheng WT, Chen CY, and Chen CM (2014). Osteoponin promoter controlled by DNA methylation: aberrant methylation in cloned porcine genome. BioMed Res. Int 2014, 327538. [PubMed: 25101273]

Storey JD, and Tibshirani R (2003). Statistical significance for genomewide studies. Proc. Natl. Acad. Sci. USA 100, 9440–9445. [PubMed: 12883005]

Sugiyama T, Galea GL, Lanyon LE, and Price JS (2010). Mechanical loading-related bone gain is enhanced by tamoxifen but unaffected by fulvestrant in female mice. Endocrinology 151, 5582–5590. [PubMed: 20943807]

Tandon M, Chen Z, and Pratap J (2014). Runx2 activates PI3K/Akt signaling via mTORC2 regulation in invasive breast cancer cells. Breast Cancer Res. 16, R16. [PubMed: 24479521]

Toyjanova J, Bar-Kochba E, López-Fagundo C, Reichner J, Hoffman-Kim D, and Franck C (2014). High Resolution, Large Deformation 3D Traction Force Microscopy. PLoS ONE 9, e90976. [PubMed: 24740435]

Tripathi S, Pohl MO, Zhou Y, Rodriguez-Frandsen A, Wang G, Stein DA, Moulton HM, DeJesus P, Che J, Mulder LC, et al. (2015). Meta- and Orthogonal Integration of Influenza "OMICs" Data Defines a Role for UBR4 in Virus Budding. Cell Host Microbe 18, 723–735. [PubMed: 26651948]

van de Vijver MJ, He YD, van't Veer LJ, Dai H, Hart AA, Voskuil DW, Schreiber GJ, Peterse JL, Roberts C, Marton MJ, et al. (2002). A gene-expression signature as a predictor of survival in breast cancer. N. Engl. J. Med 347, 1999–2009. [PubMed: 12490681]

Venet D, Dumont JE, and Detours V (2011). Most random gene expression signatures are significantly associated with breast cancer outcome. PLoS Comput. Biol 7, e1002240. [PubMed: 22028643]

Wagner EF (2002). Functions of AP1 (Fos/Jun) in bone development. Ann. Rheum. Dis 61 (Suppl 2), ii40–ii42. [PubMed: 12379619]

Yang C, Tibbitt MW, Basta L, and Anseth KS (2014). Mechanical memory and dosing influence stem cell fate. Nat. Mater 13, 645–652. [PubMed: 24633344]

Yeh AC, and Ramaswamy S (2015). Mechanisms of Cancer Cell Dormancy–Another Hallmark of Cancer? Cancer Res. 75, 5014–5022. [PubMed: 26354021]

Young DW, Hassan MQ, Yang X-Q, Galindo M, Javed A, Zaidi SK, Furcinitti P, Lapointe D, Montecino M, Lian JB, et al. (2007). Mitotic retention of gene expression patterns by the cell fate-determining transcription factor Runx2. Proc. Natl. Acad. Sci. USA 104, 3189–3194. [PubMed: 17360627]

Zaidi SK, Young DW, Montecino MA, Lian JB, van Wijnen AJ, Stein JL, and Stein GS (2010). Mitotic bookmarking of genes: a novel dimension to epigenetic control. Nat. Rev. Genet 11, 583–589. [PubMed: 20628351]

Zaidi SK, Lian JB, van Wijnen A, Stein JL, and Stein GS (2017). Mitotic Gene Bookmarking: An Epigenetic Mechanism for Coordination of Lineage Commitment, Cell Identity and Cell Growth. Adv. Exp. Med. Biol 962, 95–102. [PubMed: 28299653]

Zhang Y, Liu T, Meyer CA, Eeckhoute J, Johnson DS, Bernstein BE, Nusbaum C, Myers RM, Brown M, Li W, and Liu XS (2008). Model-based analysis of ChIP-Seq (MACS). Genome Biol. 9, R137. [PubMed: 18798982]

Zheng G, Ma Y, Zou Y, Yin A, Li W, and Dong D (2018). HCMDB: the human cancer metastasis database. Nucleic Acids Res. 46 (D1), D950–D955. [PubMed: 29088455]

Highlights

- Mechanical conditioning is associated with distinct cytoskeletal features of cells
- Mechanical conditioning is reflected in a temporal profile of chromatin accessibility
- RUNX2 promotes bone metastasis via maintenance of mechanical conditioning
- Breast tumor mechanical conditioning is associated with bone metastasis in patients

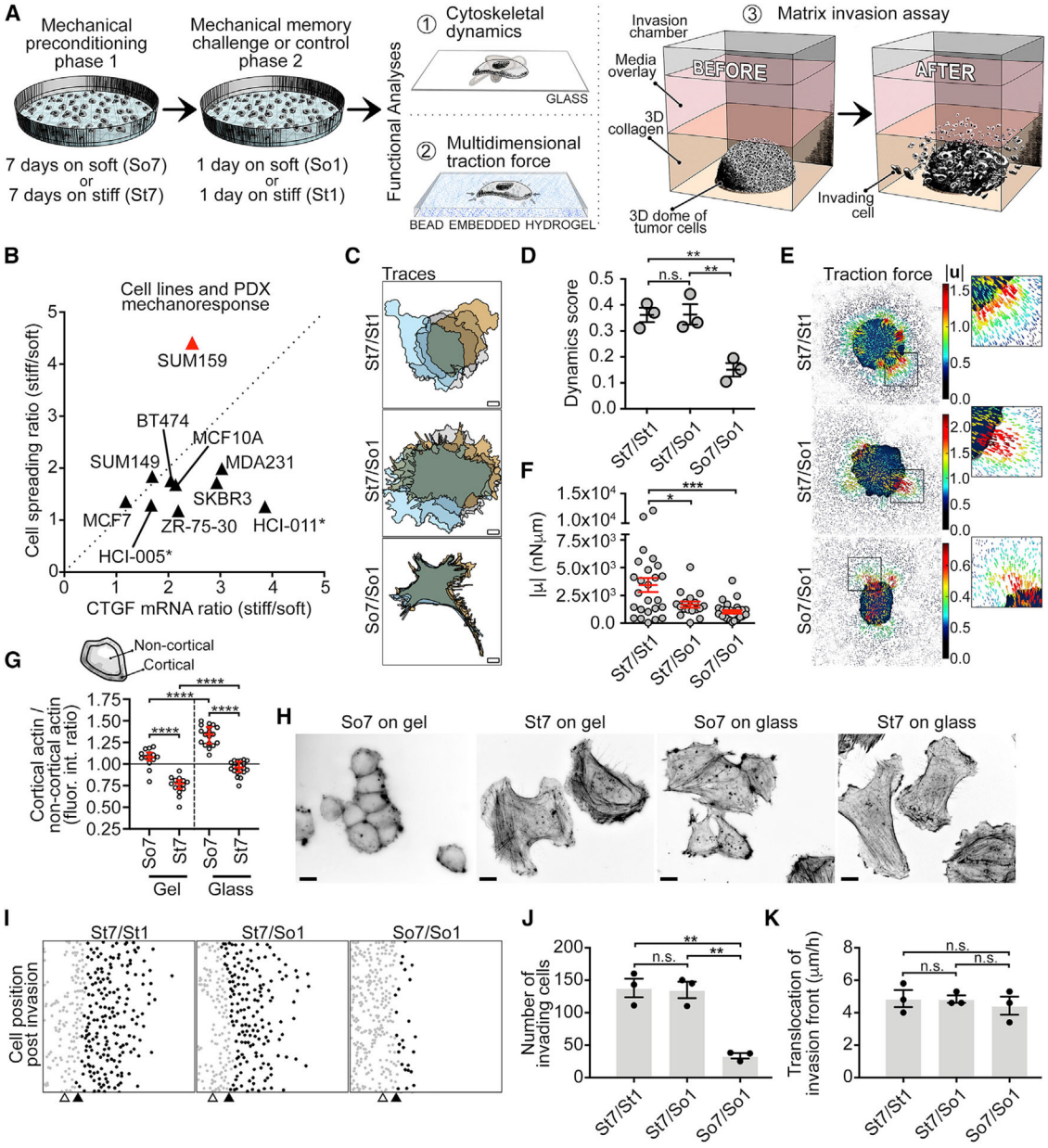

Figure 1. Mechanical conditioning manifests distinctively in cellular dynamics and invasion

(A) Schematics showing multifunctional analysis workflow for testing mechanical memory.

(B) Mechanoresponse readouts for a panel of breast cancer cell lines and patient-derived xenografts (denoted by asterisks).

(C) Dynamics (overlaid cell traces) of iRFP-Lifeact-expressing SUM159 cells preconditioned on stiff and/or soft hydrogels as indicated, showing 1-h intervals starting 10 h after plating on glass. Scale bars, 10 μm. See Video S1.

(D) Quantification of (C) (n = 36 cells in each condition from n = 3 biological replicates).

(E) Multidimensional traction force microscopy of SUM159 cells on bead-embedded 8.5 kPa gels, preconditioned on regular stiff and/or soft hydrogels, as indicated. Panels show vector maps of displacement magnitude. Heat scales (μm) show bead displacement.

(F) Quantification of (E) (n = 17–28 cells in each condition from n = 3 biological replicates). (G and H) Analysis of actin cytoskeletal structures in 7-day soft and stiff preconditioned cells before and after plating on glass for 1 day. Quantification (G) of cells *in situ* on gels and on glass, and corresponding representative images (H). Scale bar, 10 μm. (I) SUM159 cell position along invasion fronts after 16 h of live-cell tracking in 3D collagen. Cells were preconditioned on stiff and/or soft hydrogels as indicated. Gray dots, non-invasive cells; black dots, invasive cells; white triangles, invasion front at start of imaging; black triangles, invasion front at end of imaging. See Figure S1F and Video S2. (J and K) Quantification of (I) (n = 3 biological replicates with n = 3 technical replicates). Data are means ± SEMs. *$p < 0.05$, **$p < 0.01$, ***$p < 0.001$; 1-way ANOVA with Tukey's multiple comparisons test.

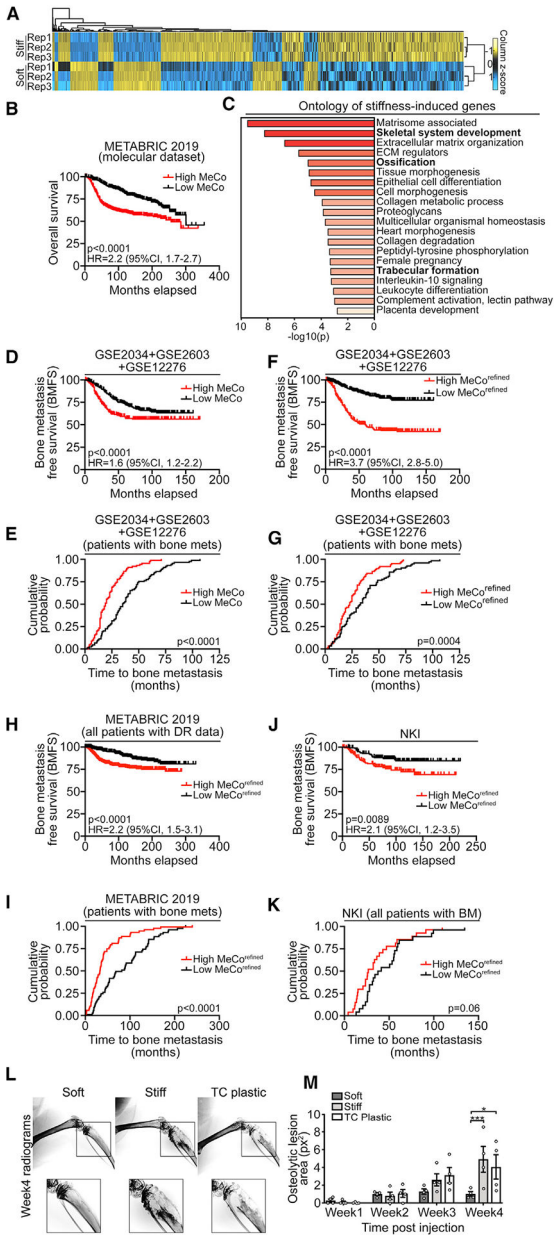

Figure 2. Primary tumor mechanical conditioning is associated with bone metastasis

(A) Heatmap of differentially regulated genes (R2-fold) from RNA-seq of 2-week soft- and stiff-preconditioned SUM159 cells, which constitute the raw mechanical conditioning genes (n = 3 biological replicates).

(B) Kaplan-Meier curve of patients in the METABRIC 2019 study (molecular dataset cohort), assigning each patient a raw mechanical conditioning (MeCo) score derived from the differential gene expression in (A) comparing upper and lower quartiles of the MeCo score (n = 476 high MeCo, 476 low MeCo). See Method details for MeCo score derivation.

(C) Metascape ontology of stiffness-induced genes (>4-fold). Bold text indicates skeletal ontologies.

(D) Kaplan-Meier curve of bone metastasis-free survival in the combined cohort, split at median MeCo score (n = 280 high MeCo, 280 low MeCo).
(E) Time to bone metastasis for patients in (D) split at median MeCo score (n = 93 high MeCo, 92 low MeCo).
(F) Kaplan-Meier curve of bone metastasis-free survival in the combined cohort, split at median $MeCo^{refined}$ score (n = 281 high $MeCo^{refined}$, 279 low $MeCo^{refined}$).
(G) Time to bone metastasis for patients in (F), split at median $MeCo^{refined}$ score (n = 93 high $MeCo^{refined}$, 92 low $MeCo^{refined}$).
(H and I) Large validation cohort for the $MeCo^{refined}$ score showing Kaplan-Meier curve of bone metastasis-free survival (H) and time to bone metastasis (I) in METABRIC 2019 (using all patients with distant relapse annotation), comparing upper and lower quartiles of $MeCo^{refined}$ score. n = 422 high $MeCo^{refined}$, 421 low $MeCo^{refined}$ in (H), and n = 65 high $MeCo^{refined}$, 64 low $MeCo^{refined}$ in (I).
(J) Kaplan-Meier curve of bone metastasis-free survival in the NKI cohort, split at median $MeCo^{refined}$ score (n = 147 high $MeCo^{refined}$, 148 low $MeCo^{refined}$).
(K) Time to bone metastasis for patients in (J), split at median $MeCo^{refined}$ score (n = 27 high $MeCo^{refined}$, 26 low $MeCo^{refined}$). The median time to metastasis for patients with high MeCo scores was 27 months, compared to 39 months for those with low MeCo scores.
(L) Radiograms of tibia from mice injected with 7-day soft-, stiff-, and plastic-preconditioned SUM159 cells, imaged 4 weeks after intracardiac injection.
(M) Quantification of (L) (n = 4 mice per group; TC, tissue culture).
Data are means ± SEMs. *$p < 0.05$, ***$p < 0.001$, ****$p < 0.0001$; 2-way ANOVA with Tukey's multiple comparisons test. Kaplan-Meier p values calculated with Wilcoxon test.

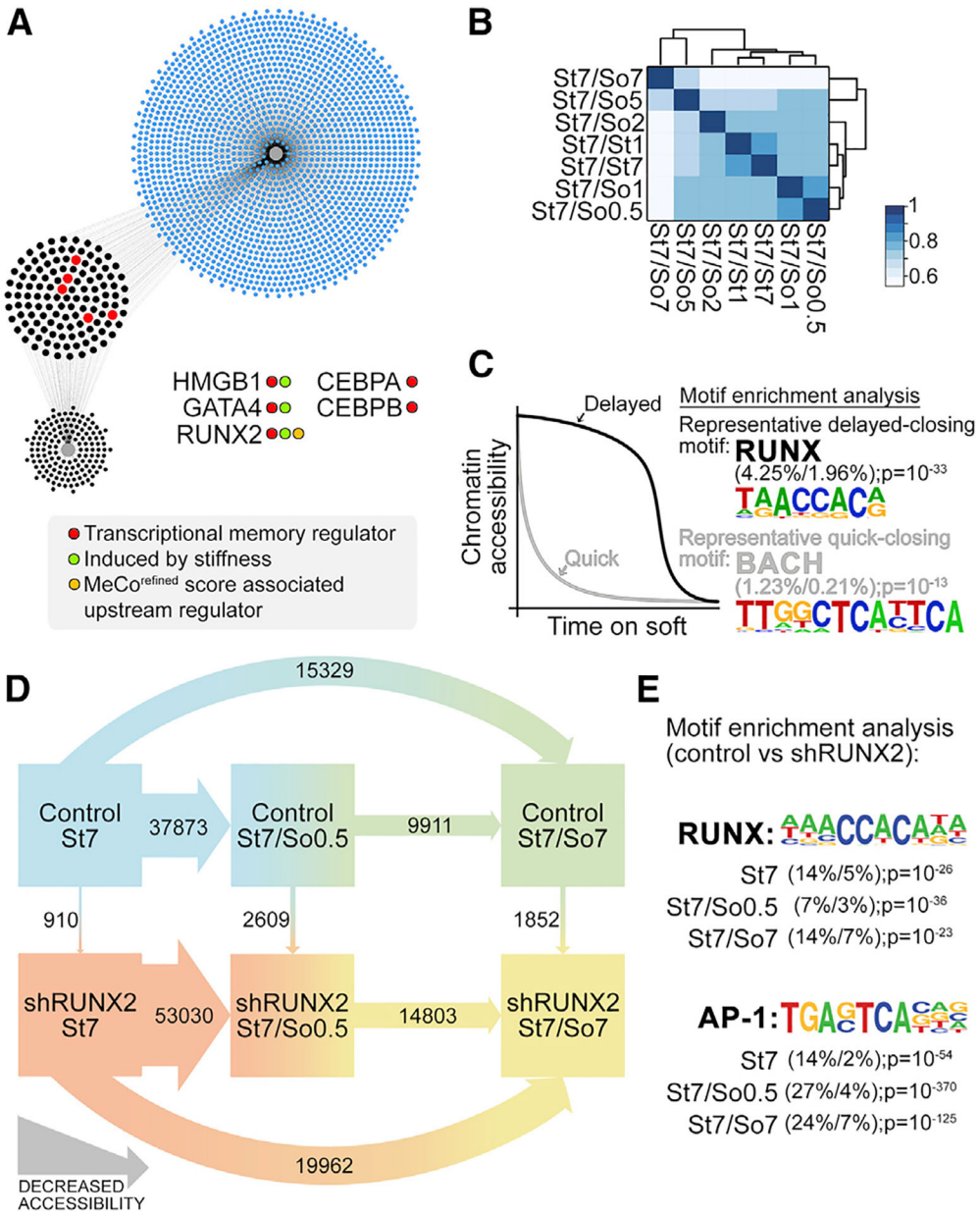

Figure 3. RUNX2 maintains mechanical conditioning in soft microenvironments

(A) Schematics of discovery approach identifying candidate drivers of mechanical memory-mediated metastasis. Gray dots, mechanically sensitive upstream regulators from RNA-seq analysis (141 genes); blue dots, Human Cancer Metastasis Database metastasis-associated genes (1,811 genes); black/red dots, intersecting genes (123 genes); red dots, intersecting genes that are known gene bookmarkers (5 genes); inset shows further characterization. See Method details for in-depth description.

(B) Heatmap showing clustering of ATAC-seq samples; scale shows Jaccard index. See Figure S4A for sample annotation.

(C) Graphic representation of change in chromatin accessibility over time after changing the mechanical environment; inset shows RUNX and BACH family motifs as representative of

the significantly enriched motifs in the delayed-closing and quick-closing sites, respectively (motifs analysis performed by HOMER).

(D) The number of pairwise differentially decreased accessibility sites are shown consequent of RUNX2-knockdown (vertical arrows) and longitudinally upon transition to soft matrix (horizontal arrows). Data represent 3 biological replicates per condition.

(E) Top enriched motifs are shown for the vertical comparisons in (D), where the first percentage is the number of differential peaks with the motif and the second is the number of GC-matched random genomic sequences with motif.

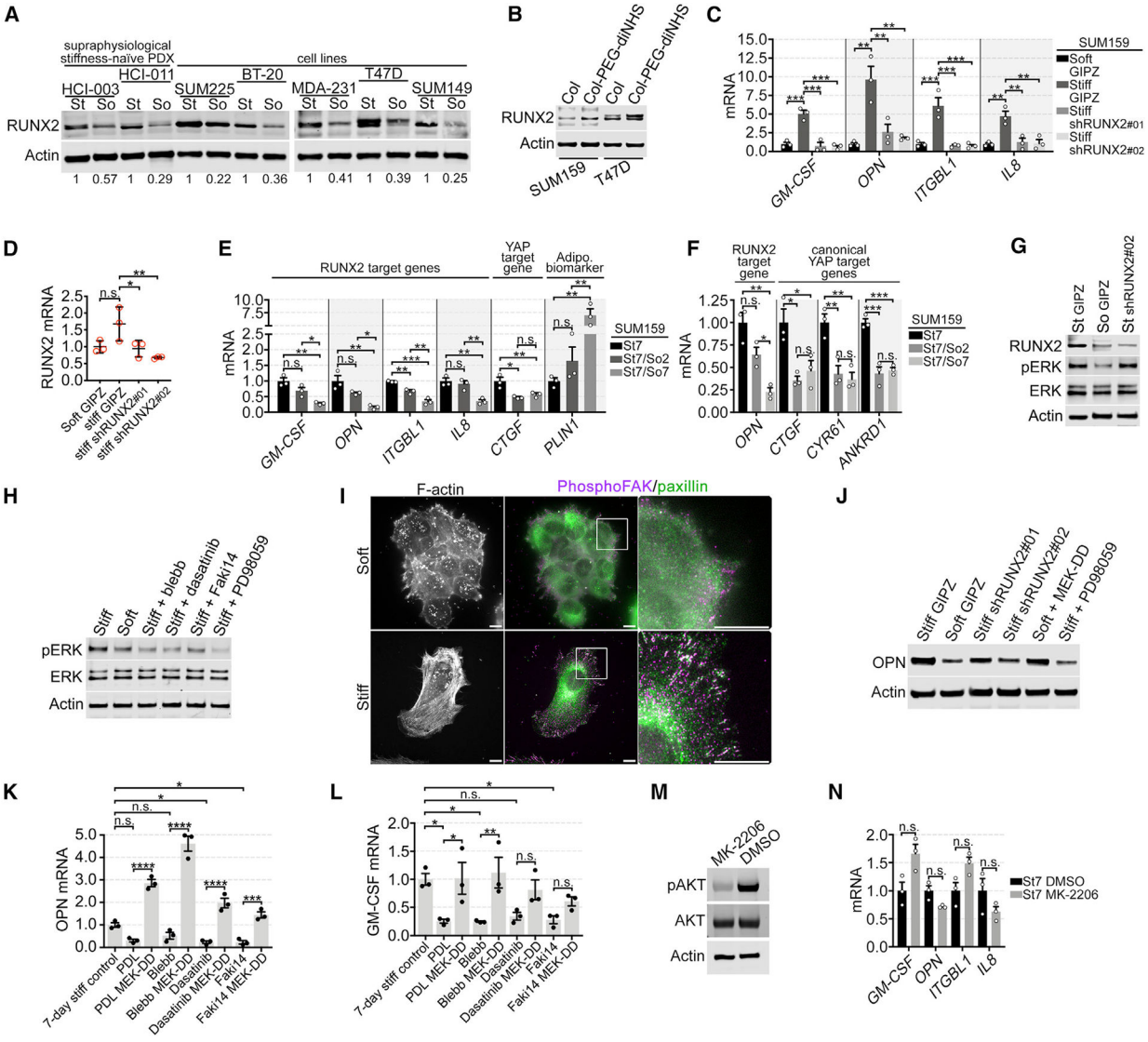

Figure 4. RUNX2 is activated by matrix stiffness via mechanotransduction

(A) Immunoblot of RUNX2 in patient-derived xenograft (PDX) primary cells and breast cancer cell lines, preconditioned on soft and stiff hydrogels for 7 days (representative of n = 2 biological replicates).

(B) Immunoblot of RUNX2 in SUM159 and T47D cells cultured for 7 days in 3D matrix consisting of soft 1.0 mg/mL rat-tail collagen-I, or stiff 1.0 mg/mL rat-tail collagen-I crosslinked with PEG-di(NHS) to stiffen the collagen lattice without changing ligand density (representative of n = 3 biological replicates).

(C) qRT-PCR of 4 RUNX2 target genes in SUM159 cells preconditioned for 7 days on soft and stiff hydrogels with non-targeting small hairpin RNA (shRNA) (GIPZ), or on stiff hydrogels with 2 shRNAs targeting RUNX2 (n = 3 biological replicates). Data are means ± SEMs. *p < 0.05, **p < 0.01, ***p < 0.001; 1-way ANOVA with Tukey's multiple comparisons test.

(D) qRT-PCR of RUNX2 in SUM159 cells preconditioned for 7 days on soft and stiff hydrogels with non-targeting shRNA (GIPZ), or on stiff hydrogels with 2 shRNAs targeting RUNX2 (n = 3 biological replicates). *p < 0.05, **p < 0.01, ***p < 0.001, ****p < 0.0001; 1-way ANOVA with Sidak's multiple comparisons test.
(E) qRT-PCR of RUNX2 and 4 target genes, plus CTGF (YAP target) and PLIN1 (adipogenic biomarker) in SUM159 cells preconditioned, as indicated (n = 3 biological replicates). Data are means ± SEMs. *p < 0.05, **p < 0.01, ***p < 0.001; 1-way ANOVA with Tukey's multiple comparisons test.
(F) qRT-PCR of the RUNX2 gene target *OPN*, and 3 YAP targets—*CTGF*, *CYR61*, and *ANKRD1*—in SUM159 cells preconditioned as indicated, and without media change for 48 h before sample collection (n = 3 biological replicates). Data are means ± SEMs. *p < 0.05, **p < 0.01, ***p < 0.001; 1-way ANOVA with Tukey's multiple comparisons test.
(G) Immunoblot of RUNX2, ERK, and pERK in SUM159 cells stably expressing lentiviral shRUNX2 or GIPZ (non-targeting control), preconditioned for 7 days on soft or stiff hydrogels (representative of n = 3 biological replicates).
(H) Immunoblot of pERK and ERK in SUM159 cells cultured on stiff hydrogels with 20 μM PD98059, 30 μM blebbistatin, 100 nM dasatinib, 1 μM Faki14, or DMSO for 1 h before lysis (representative of n = 3 biological replicates).
(I) Immunofluorescence of pFAK, paxillin, and F-actin in SUM159 cells cultured on stiff or soft hydrogels for 7 days. Scale bar, 10 μm.
(J) Immunoblot of OPN in SUM159 cells preconditioned for 7 days on soft and stiff hydrogels with non-targeting shRNA (GIPZ), on stiff hydrogels with 2 shRNAs targeting RUNX2, on soft hydrogels with constitutively active MEK-DD expression, or on stiff hydrogels with MEK inhibitor PD98059 (20 μM) (representative of n = 3 biological replicates).
(K and L) qRT-PCR of OPN (K) and GM-CSF (L) in SUM159 cells preconditioned for 7 days on stiff hydrogels conjugated with either poly D-lysine (PDL) to reduce integrin binding, or collagen conjugated with DMSO (control), 30 μM blebbistatin, 100 nM dasatinib, or 1 μM Faki14 in media changed every other day (n = 3 biological replicates). Data are means ± SEMs and normalized to 7-day stiff controls. *p < 0.05, **p < 0.01, ***p < 0.001, ****p < 0.0001; 1-way ANOVA with Sidak's multiple comparisons test.
(M) Immunoblot showing phospho-AKT levels in SUM159 cells treated with DMSO (control) or AKT inhibitor (1 μM MK-2206) (representative of n = 2 biological replicates).
(N) qRT-PCR of RUNX2 target genes in SUM159 cells preconditioned for 7 days on stiff hydrogels and treated with DMSO or 1 μM AKT inhibitor MK-2206 (n = 3 biological replicates). Data are means ± SEMs. Multiple t test with Holm-Sidak multiple comparisons; adjusted p values are not significant (n.s.).

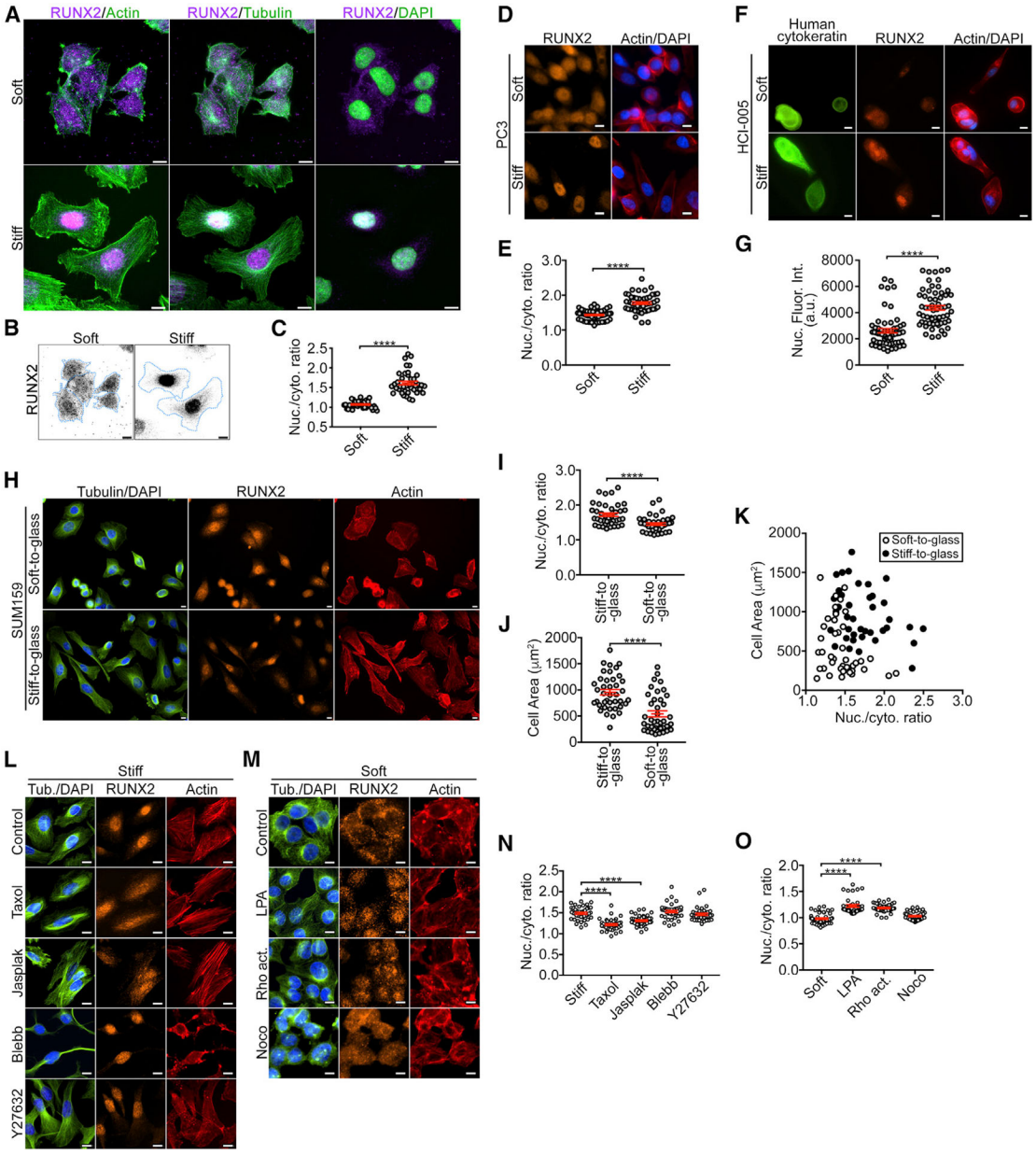

Figure 5. RUNX2 nuclear localization is regulated by matrix stiffness

(A) Immunofluorescence staining of RUNX2 in SUM159 cells on soft and stiff hydrogels. Scale bars, 10 μm.

(B) Immunofluorescence corresponding to Figure 4G. Cell boundaries are delineated in blue. Scale bars, 10 μm.

(C) Quantification of (B) (n = 40 cells in each condition from n = 3 biological replicates). ****p < 0.0001; 2-tailed unpaired Student's t test.

(D and E) Immunofluorescence staining (D) and quantification of nuclear localization (E) of RUNX2 in PC3 prostate cancer cells (n = 50 cells each from n = 3 biological replicates).

(F and G) Immunofluorescence staining of RUNX2 (F) and quantification of nuclear intensity of RUNX2 in CK^+ cells (G) in supraphysiological stiffness-naive patient-derived xenograft HCI-005 tumor cells (n = 60 cells each from n = 3 biological replicates).
(H) Immunofluorescence staining in SUM159 cells, preconditioned on soft and stiff hydrogels for 7 days before transferring to collagen-coated glass for 3 h.
(I and J) Quantification of nuclear RUNX2 (I) and cell area (J) from cells in (H). Data are means ± SEMs. ****p < 0.0001; 2-tailed unpaired Student's t test.
(K) Correlation analysis of (I) and (J), showing no positive intracellular correlation between cell spreading and nuclear RUNX2 in either soft- or stiff-preconditioned cells spreading on glass (n = 40 cells each from n = 3 biological replicates). Soft-to-glass Pearson's r = −0.31 (not significant [n.s.]); stiff-to-glass Pearson's r = −0.30 (n.s.).
(L) Immunofluorescence staining of RUNX2 in SUM159 cells preconditioned for 7 days on stiff hydrogels, treated with DMSO (control), 1 μM taxol, 50 nM jas-plakinolide, 30 μM blebbistatin, or 20 μM Y27632, added 3 h before fixation. Scale bars, 10 μm.
(M) Immunofluorescence staining of RUNX2 in SUM159 cells preconditioned for 7 days on soft hydrogels, with DMSO (control), 1 μg/mL lysophosphatidic acid (LPA), 10 μg/mL Rho Activator II, or 10 μM nocodazole, added 3 h before fixation. Scale bars, 10 μm.
(N) Quantification of (L) (n R 40 cells each condition from n = 3 biological replicates).
(O) Quantification of (M) (n R 40 cells each condition from n = 3 biological replicates). Data are means ± SEMs. ****p < 0.0001; 1-way ANOVA with Dunnett's multiple comparisons test.

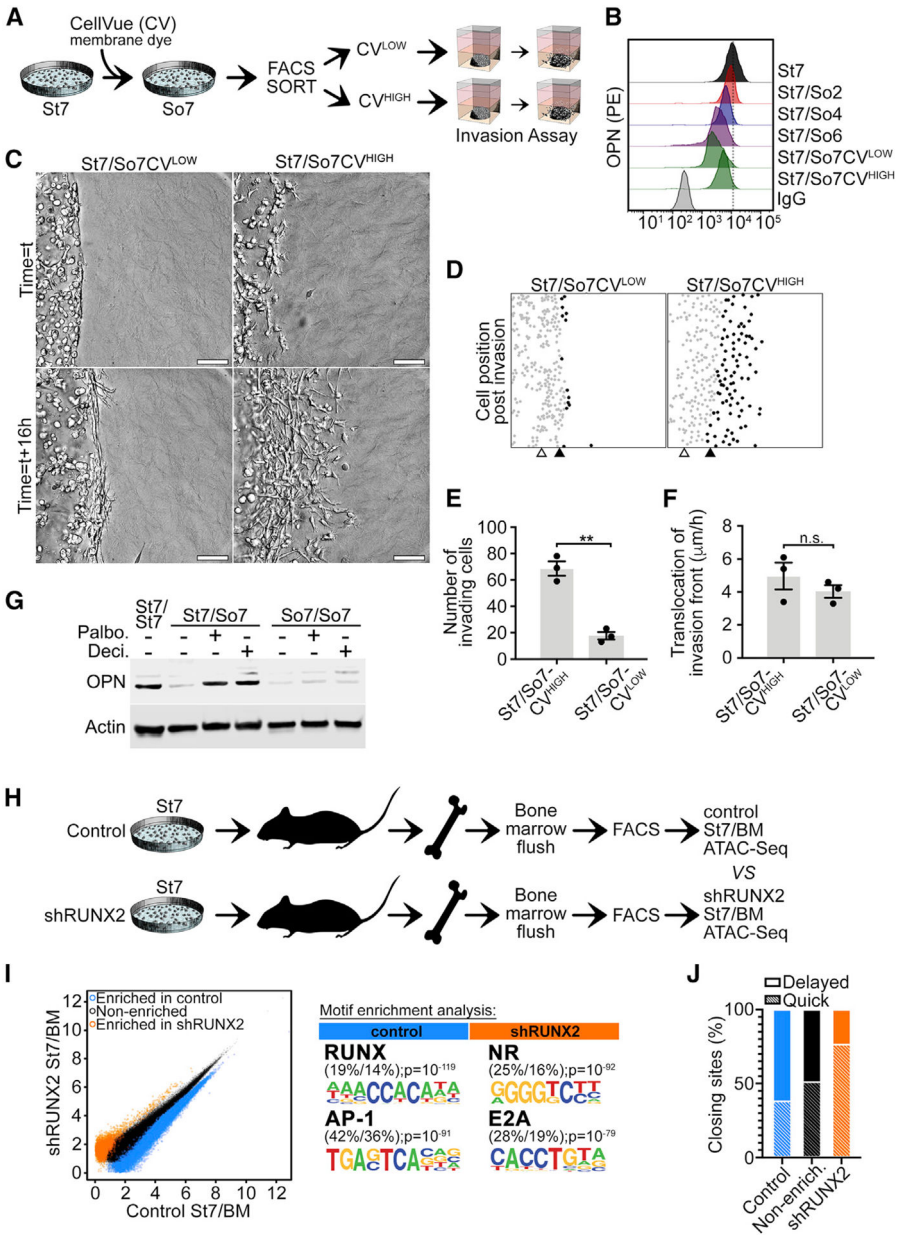

Figure 6. RUNX2 is associated with proliferation-sensitive mechanical conditioning, which is maintained in bone marrow (BM) resident cancer cells

(A) Schematics showing strategy to enrich high-proliferative cells (CV^{LOW}) versus low-proliferative cells (CV^{HIGH}).

(B) Time course of mechanical memory loss, showing flow cytometry of SUM159 cells preconditioned as indicated, sorted, and stained for OPN (n = 3 biological replicates). See Figure S6A.

(C) Enhanced depth-of-focus differential interference contrast (DIC) images of high-proliferative cells (CV^{LOW}) versus low-proliferative cells (CV^{HIGH}) before and after 16 h of invasion in 3D collagen.

(D–F) SUM159 cell position (D) and quantification of single-cell invasion (E) and translocation of invasion front (F) after 16 h of live-cell tracking in 3D collagen. Gray dots,

non-invasive cells; black dots, invasive cells; white triangles, invasion front at start of imaging; black triangles, invasion front at end of imaging. See Video S3 (n = 3 biological replicates with n = 3 technical replicates). Data are means ± SEMs. **p < 0.01; 2-tailed unpaired Student's t test.

(G) Immunoblot of OPN showing memory extension in SUM159 cells treated with DMSO, palbociclib (2.5 μM; CDK4/6 inhibitor) or decitabine (7 μM; DNMT1 inhibitor) on soft hydrogels for 7 days in phase 2, after stiff- or soft-preconditioning for 7 days in phase 1. Drugs were added only in phase 2 (representative n = 3 biological replicates).

(H) Schematic of experiment for injection of stiff preconditioned SUM159/GFP^+ control or shRUNX2 cells into mice. BM was collected after 7 days, and then GFP^+ cancer cells were sorted and assayed by ATAC-seq (n = 3 biological replicates).

(I) Differentially accessible sites between control and shRUNX2 are shown by scatterplot (fold change > 1.7; $p < 10^{-6}$), and motifs enriched in corresponding subsets are shown in the inset.

(J) Proportions of quick and delayed closing sites (defined in Figure 3C) are shown for each set from (I).

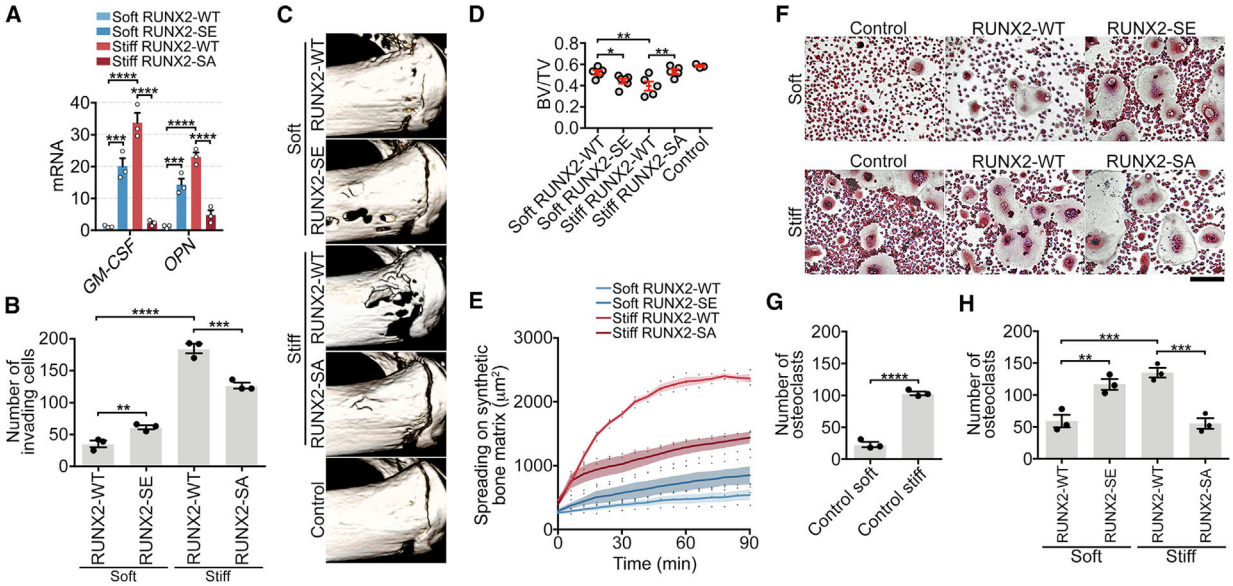

Figure 7. RUNX2-mediated mechanical conditioning instructs bone metastasis

(A) qRT-PCR of RUNX2 target genes in SUM159 cells overexpressing RUNX2-WT, RUNX2-SE, or RUNX2-SA, preconditioned for 7 days on soft or stiff hydrogels (n = 3 biological replicates).

(B) Quantification of invasion of SUM159 cells preconditioned as indicated in (A) (n = 3 biological replicates with n = 3 technical replicates). See Figures S6L–S6N and Video S6.

(C) Micro-CT 3D reconstructions of proximal tibia from mice 4 weeks after intracardiac injection of SUM159 cells preconditioned as in (A) or no cancer cells (control).

(D) Micro-CT analysis of bone volume from mice in (C) (*n*, mice; soft RUNX2-WT 5; soft RUNX2-SE 6; stiff RUNX2-WT 5; stiff RUNX2-SA 5; control 3).

(E) Time course of SUM159 cells spreading on synthetic bone matrix, preconditioned as in (A) (n = 36 cells in each condition from n = 3 biological replicates). See Video S7. Shaded regions are means ± SEMs. ****p < 0.0001; 2-way ANOVA with Tukey's multiple comparisons test.

(F) Tartrate-resistant acid phosphatase (TRAP) staining of RAW264.7 cells after 7 days' incubation: 4 days with 50 ng/mL RANKL in growth media, and then 3 days with 50% SUM159-conditioned media (CM) + 50% growth media. CM was collected 24 h after addition to hydrogels with equal SUM159 cell counts in each experimental group. Scale bar, 100 μm.

(G and H) Quantification of (F) (n = 3 biological replicates with n = 3 technical replicates). Two-tailed unpaired Student's t test.

Data are means ± SEMs. *p < 0.05, **p < 0.01, ***p < 0.001, ****p < 0.0001; 1-way ANOVA with Holm-Sidak's multiple comparisons test, except for (E) and (G).

KEY RESOURCES TABLE

REAGENT or RESOURCE	SOURCE	IDENTIFIER
Antibodies		
RUNX2	Sigma	Cat: HPA022040
RUNX2	Cell Signaling Technology	Cat: 8486S
Tubulin	Sigma	Cat: T9026
Paxillin	BD Biosciences	Cat: 612405
pFAK	Thermo	Cat: 44-625G
OPN	Abcam	Cat: ab8448
OPN	Abcam	Cat: ab91655
OPN-PE	Abcam	Cat: ab210835
ERK	Santa Cruz	Cat: sc-93-G
pERK	Cell Signaling Technology	Cat: 4377S
AKT	Cell Signaling Technology	Cat: 2920S
pAKT	Cell Signaling Technology	Cat: 4058S
Actin	ProteinTech Group	Cat: 66009-1
Alexa Fluor goat anti-rabbit 680	Invitrogen	Cat: A27042
Alexa Fluor goat anti-mouse 790	Invitrogen	Cat: A28182
Biological samples		
Patient-derived xenograft HCI-003	Alana Welm, Huntsman Cancer Institute	N/A
Patient-derived xenograft HCI-005	Alana Welm, Huntsman Cancer Institute	N/A
Patient-derived xenograft HCI-011	Alana Welm, Huntsman Cancer Institute	N/A
Peripheral blood mononuclear cells	This paper	N/A
MS-SKBR3.1 sensitized cells	This paper	N/A
Chemicals, peptides, and recombinant proteins		
3-aminopropyltrimethoxy silane	Sigma	Cat: 13822-56-5
Sulfo-SANPAH	Biovision	Cat: 2324
Rat-tail collagen I	Corning	Cat: 354249
PEG-di(NHS)	Polysciences	Cat: 26115
pCMV-msRUNX2	Gerard Karsenty, Columbia	N/A
pCIG3	Gift from the Goodrum Lab, U Arizona	Addgene Cat: 78264
pCIG3-msRUNX2	This paper	N/A
pCIG3-msRUNX2-S301A-S319A	This paper	N/A
pCIG3-msRUNX2-S301E-S319E	This paper	N/A
human RUNX2-I	Genecopoeia	Cat: EX-I2457-Lv105
pCIB	Puleo et al., 2019	Addgene Cat: 119863

REAGENT or RESOURCE	SOURCE	IDENTIFIER
pCIB-hsRUNX2	This paper	N/A
pCIB-hsRUNX2-S280A-S298A	This paper	N/A
pCIB-hsRUNX2-S280E-S298E	This paper	N/A
pBabe-Puro-MEK-DD	Gift from the Hahn Lab, Dana Farber Cancer Institute	Addgene Cat: 15268
pLenti Lifeact-iRFP670-BlastR	Padilla-Rodriguez et al., 2018	Addgene Cat: 84385
shRUNX2#01	Dharmacon	Cat: V2LHS_15065
shRUNX2#02	Dharmacon	Cat: V2LHS_223856
psPAX2	Gift from Didier Trono	Addgene Cat: 12260
pMD2.G	Gift from Didier Trono	Addgene Cat: 12259
pCL-Ampho	Novus	Cat: NBP2-29541
pGIPZ	Sourav Ghosh, Yale	N/A
HI-FBS	GIBCO	Cat: A3840201
FBS	GIBCO	Cat: 26140079
Blebbistatin	Sigma	Cat: 203391
Dasatinib	Tocris	Cat: 6793
Faki14	Tocris	Cat: 3414
CellVue Claret far-red membrane label	Sigma	Cat: MINCLARET
Matrigel	Corning	Cat: 356234
Palbociclib	Sigma	Cat: 571190-30-2
Decitabine	Sigma	Cat: 189825
PD98059	Tocris	Cat: 1213
Critical commercial assays		
LIVE/DEAD Viability/ Cytotoxicity	Thermo Fisher	Cat: L3224
MycoAlert Mycoplasma screening	Biotool	Cat: LT07-218
Quikchange II	Agilent	Cat: 200523
PKH67 Green Fluorescent Cell Linker	Sigma	Cat: MINI67-1KT
Isolate II RNA kit	Bioline	Cat: BIO-52072
XLA script cDNA kit	Quanta Biosciences	Cat: 95048
GM-CSF Human SimpleStep ELISA kit	Abcam	Cat: ab174448
Acid Phosphatase, Leukocyte (TRAP) kit	Sigma	Cat: 387A
Osteo Assay	Corning	Cat: 3987
Deposited data		
ATAC-seq, RNA-seq	This paper	GEO: GSE127887
NKI clinical dataset	van de Vijver et al., 2002	https://www.nejm.org/doi/full/10.1056/NEJMoa021967
METABRIC 2019 clinical dataset	Rueda et al., 2019	http://www.nature.com/articles/s41586-019-1007-8
GSE2034 clinical dataset	Bos et al., 2009	GEO: GSE2034
GSE2603 clinical dataset	Bos et al., 2009	GEO: GSE2603

REAGENT or RESOURCE	SOURCE	IDENTIFIER
GSE12276 clinical dataset	Bos et al., 2009	GEO: GSE12276
SI Tables and Data Set 1	This paper	http://doi.org/10.17632/kvzhkpb8yd.1
Experimental models: cell lines		
SUM149	Joan Brugge, Harvard	N/A
SUM159	Joan Brugge, Harvard	N/A
MCF10A	Joan Brugge, Harvard	N/A
MDA-MB-231	Joan Brugge, Harvard	N/A
HEK293T	Joan Brugge, Harvard	N/A
MCF7	Joan Brugge, Harvard	N/A
BT474	Joan Brugge, Harvard	N/A
T47D	Joan Brugge, Harvard	N/A
MCF10A-Neu	Cheuk Leung, University of Minnesota	N/A
SKBR3	ATCC	Cat: HTB-30
PC3	ATCC	Cat: CRL-1435
BT-20	ATCC	Cat: HTB-19
ZR-75-30	ATCC	Cat: CRL-1504
RAW264.7	ATCC	Cat: TIB-71
Experimental models: organisms/strains		
NOD.Cg-Prkdcscid Il2rgtm1Wjl/SzJ mice	JAX	Cat: 005557
NOD.Cg-Prkdcscid/J	JAX	Cat: 001303
Oligonucleotides		
See SI Tables on Mendelay Data (Table S8)	This paper	http://doi.org/10.17632/kvzhkpb8yd.1
Software and algorithms		
FIDVC	Bar-Kochba et al., 2015	https://idp.springer.com/authorize?response_type=cookie&client_id=springerlink&redirect_uri=https%3A%2F%2Flink.springer.com%2Farticle%2F10.1007%2Fs11340-014-9874-2
Inveon Research Workplace	Siemens	https://www.siemens.com
AMIView	Spectral Instruments	https://spectralinvivo.com
GREAT v4.0.4	McLean et al., 2010	http://great.stanford.edu/public/html/
NIS-Elements	Nikon	https://www.microscope.healthcare.nikon.com/products/software/nis-elements
STAR	Dobin et al., 2013	https://code.google.com/archive/p/rna-star
HOMER	Heinz et al., 2010	http://homer.ucsd.edu/homer/
DESeq		https://www.huber.embl.de/users/anders/DESeq/
FACSDiva	BD Biosciences	https://www.bdbiosciences.com/en-us/instruments/research-instruments/research-software/flowcytometry-acquisition/facsdiva-software
Bowtie2		http://www.nature.com/articles/nmeth.1923
MACS2	Zhang et al., 2008	http://genomebiology.biomedcentral.com/articles/10.1186/gb-2008-9-9-r137
BEDTools		https://code.google.com/archive/p/bedtools
Prism v8.0	GraphPad	https://www.graphpad.com/scientific-software/prism/